Development of New Front Side Metallization Method of Aluminum Electroplating for Silicon Solar Cell

by

Laidong Wang

A Dissertation Presented in Partial Fulfillment
of the Requirements for the Degree
Doctor of Philosophy

Approved December 2017 by the
Graduate Supervisory Committee:

Meng Tao, Chair
Dragica Vasileska
Michael Kozicki
Michael Goryll

ARIZONA STATE UNIVERSITY

May 2018

ABSTRACT

In this thesis, the methods of aluminum electroplating in an ionic liquid for silicon solar cell front side metallization were studied. It focused on replacing the current silver screen printing with an alternative metallization technology using a low-cost Earth-abundant metal for mass production, due to the high cost and limited availability of silver. A conventional aluminum electroplating method was employed for silicon solar cells fabrication on both p-type and n-type substrates. The highest efficiency of 17.9% was achieved in the n-type solar cell with a rear junction, which is comparable to that of the same structure cell with screen printed silver electrodes from industrial production lines. It also showed better spiking resistant performance than the common structure p-type solar cell. Further efforts were put on the development of a novel light-induced plating of aluminum technique. The aluminum was deposited directly on a silicon substrate without the assistance of a conductive seed layer, thus simplified and reduced the process cost. The plated aluminum has good adhesion to the silicon surface with the resistivity as low as 4×10^{-6} Ω-cm. A new demo tool was designed and set up for the light-induced plating experiment, aiming to utilize this technique in large-size solar cells fabrication and mass production. Besides the metallization methods, a comprehensive sensitivity analysis for the efficiency dispersion in the production of crystalline-Si solar cells was presented based on numerical simulations. Temperature variation in the diffusion furnace was the most significant cause of the efficiency dispersion. It was concluded that a narrow efficiency range of ±0.5% absolute is achievable if the emitter diffusion temperature is confined to a 13˚C window, while other cell parameters vary within their normal windows. Possible methods to minimize temperature variation in emitter diffusion were proposed.

ACKNOWLEDGMENTS

I would like to thank Dr. Meng Tao for his remarkable support and guidance, without which this would not be possible. His diligent involvement, systematic supervision, and his wealth of creativity benefit me a lot during my Ph.D. study and for my future career. I would also like to acknowledge Dr. Dragica Vasileska, Dr. Michael Kozicki, and Dr. Michael Goryll for serving in my doctoral committee. I sincerely appreciate their valuable inputs for my research. I would like to thank Dr. Clarence J. Tracy for sharing his valuable experience in the fabrication of silicon solar cells.

I am very grateful to Dr. Haifeng Zhang, who introduced me to the group and helped me a lot in discussion and in experiments. I am also grateful to Dr. Wen-Cheng Sun, who started the project and designed the experiment. He lead me into the process of aluminum electroplating. I would like to acknowledge my colleagues Dr. Wen-His Huang, Dr. Woo Jun Shin, and Dr. Joseph Azzolini in the research group. They helped me a lot with many experiments and tests. I benefited greatly from the technical discussions with them, which inspired many wonderful ideas. Thanks to Lewis Ricci for his effort to work on my project further.

I would like to express my great thanks to my family. My parents supported me a lot even though they lived abroad. My wife, Dr. Jiaquan Xu, supported me when I was struggling to the make the breakthrough.

This work was supported by the U.S. National Science Foundation under grant no. 1336297. Hareon Solar and Canadian Solar provided solar cell samples to our group.

TABLE OF CONTENTS

Page

CHAPTER Page

LIST OF TABLES

Table Page

LIST OF FIGURES

Figure Page

Figure Page

Figure Page

Figure Page

1. INTRODUCTION

1.1 Motivation

Climate change is one of the most significant and severe challenges for human beings on this planet. High temperature, rising seas, increased risk of storms, droughts, and floods, are continuously threatening everyone in the world. Based on the IPCC report [1], the climate change is attributed to the emission of greenhouse gas and global warming. In order to prevent or alleviate the damages from the climate change, scientists and researchers proposed to limit the global warming to 1.5ºC above pre-industrial levels in the Paris agreement in 2015 [2]. The world is searching for alternative energy resources to replace fossil fuels. Solar energy, with the development of photovoltaic (PV) industry, is a promising candidate in the renewable energies for current and future applications [3].

Among different types of solar cells, the crystalline-silicon (c-Si) solar cell is a dominant product. By the end of 2016, the global PV industry has reached >90 GWp module production capacity with 90% on crystalline silicon solar cells [4]. In order to compete with conventional fuels energy sources and other renewable energies, manufacturers are forced to accelerate the cost reduction and increase the cell efficiency. The PV industry links cost reduction measures with enhanced cell performance by improving Si wafer quality, front and rear sides metallization, refined layout, and module packages.

The cost of c-Si modules can be divided into 40% for the module manufacturing process, 40% for the wafer, and 20% for the solar cell fabrication [5]. As of January 2018, the price is down to ~$0.31/Wp for c-Si modules then ~$0.194/Wp for multi-Si cells [6]. Silver (Ag) paste, most used in front contact metallization for commercial c-Si solar cells,

costs ~$0.011/Wp, taking up to ~5.67% of the cell, or ~13% of the non-Si cell price[4]. However, there are still drawbacks preventing Ag in the terawatt-level photovoltaic application. For one thing, the Ag is a precious metal with a high price which fluctuates frequently. It was around three times higher than the current price in 2011 when the PV industry suffered from it [7]. Though it is hard to predict the price in the future, no one expects the price will keep low with the increasingly strong demand in PV industry. For the other thing, the limited global reserve of Ag may not meet the growing demand from the PV industry. The known reserve of Ag is 570000 metric tons according to the mineral commodity summaries published by U.S. Geological Survey in 2017 [8]. The average use of Ag in one cell is 90mg/cell (for a 19.6% mc-Si PERC cell). 2,600 tonnes of Ag was consumed for 73 GW_p solar capacity in 2016, so the global reserve of Ag may only output 16 TWp solar capacity. In International Energy Outlook 2017, the projected energy demand in 2040 is 736 quadrillion Btu which equals to 197 TWp capacity [3]. Thus, the total energy these cells can fulfill only 8.1% of the energy demand.

Though Ag consumption is continuously reduced with advanced techniques in manufacturing, it is required to replace Ag with an Earth-abundant, low-cost, and high-conductive material. Table 1.1 shows the metals sorted by resistivity [9]. Among these metals, Cu and Al are possible candidates with low resistivity and a large reserve. Cu is used in mass production to some extent and expected to climb to 5% in 2019. Compared to Cu, Al is another promising candidate to replace Ag as the front electrode in c-Si solar cells. In this work, the aluminum electrolytic metallization methods were investigated and developed.

Table 1.1 Reserve and cost of low resistive metals

	Resistivity (Ω-cm)	Reserve (tonnes)	**Cost ($/lb)**
Ag	1.59×10^{-6}	5.7×10^{5}	281.6
Cu	1.68×10^{-6}	7.2×10^{8}	2.67
Al	2.82×10^{-6}	$5.5\sim7.5\times10^{10}$	0.87
W	5.60×10^{-6}	3.1×10^{6}	11.45
Zn	5.90×10^{-6}	2.2×10^{8}	1.30
Ni	6.99×10^{-6}	7.8×10^{7}	4.58
Sn	10.9×10^{-6}	4.7×10^{6}	9.33
Ti	42.0×10^{-6}	7.4×10^{6}	1.57

1.2 Chapter Outline

In this chapter, the challenge in climate change and the significance to develop solar cells are explained. The cost structure for manufacturing the mainstream Si solar cell is shown and Ag paste takes up a large amount of non-Si material cost. The bottlenecks of Ag in the future terawatt PV application are explained. Various metal candidates to replace Ag are compared based on resistivity, cost, and availability. Besides wide investigated Cu, we focus on Al for Si solar cell front electrode metallization.

In Chapter 2, the basic structure and operation theory is described, including the typical commercial Si solar cell, characterization parameters, and loss mechanisms. The typical structure is also used throughout this work in further research compare. The loss mechanisms include optical loss and electrical loss for the cell side and mismatch loss for the module side.

In Chapter 3, the manufacturing of Si solar cell process flow is introduced. It includes the current industrial methods for saw damage removal and texturing, emitter diffusion, edge isolation, anti-reflection coating, and contact metallization. New emerging methods to improve the performance or reduce the cost in some steps are also introduced.

In Chapter 4, the development of a Si solar cell with electroplated Al as the front electrode is reported. The experiment is carried out on a half-processed p-type solar cell substrate in an ionic liquid. The theory of Al electroplating reactions in the ionic liquid is introduced first. The fabricated solar cell is tested and showing reasonable performance. A modified structure on an n-type substrate is also proposed and fabricated. The final cell is showing spiking-resistant performance and the efficiency is comparable to solar cells from commercialized production lines.

In Chapter 5, the light-induced plating of Al on Si substrate in an ionic liquid is reported. Compared to the traditional electroplating described in chapter 4, the new method gets rid of Ni seed layer and allows Al to be directly plated on Si surface, which simplifies the process and reduces the cost. The deposited Al is characterized by SEM and EDX. The resistivity is measured and compared with that of traditional electroplated Al and screen-printed Ag. The suitable light source and monitoring method are also discussed.

In Chapter 6, the efficiency dispersion in mass production of Si solar cell is analyzed with numerical simulation. A comprehensive and quantitative analysis on the effects of various factors is performed. The fluctuation of diffusion temperature has a dominant effect on the final efficiency. It is proposed the efficiency can be controlled within 1% absolute if the temperature is maintained within a certain range.

2. SILICON SOLAR CELL STRUCTURE AND OPERATION

2.1 Structure

The solar cell is an electrical device which converts incidence of sunlight directly into electricity. Basically, a Si solar cell device is a large area semiconductor PN junction, as shown in Fig. 2.1 [10]. When sunlight shining onto solar cell is absorbed, photons with higher energy than the semiconductor bandgap excite electron-hole pairs (EHP). The EHPs generated or diffused into the depletion region of PN junction are separated by the built-in electric field, in which electrons are pushed to N region while holes are pulled to P region before the recombination occurs. Electrons and holes accumulated in each region lead to the voltage difference between both ends of the PN junction. When an external electrical load is applied, a current driven by the voltage flows through the circuit and provide output power. This is the photovoltaic effect.

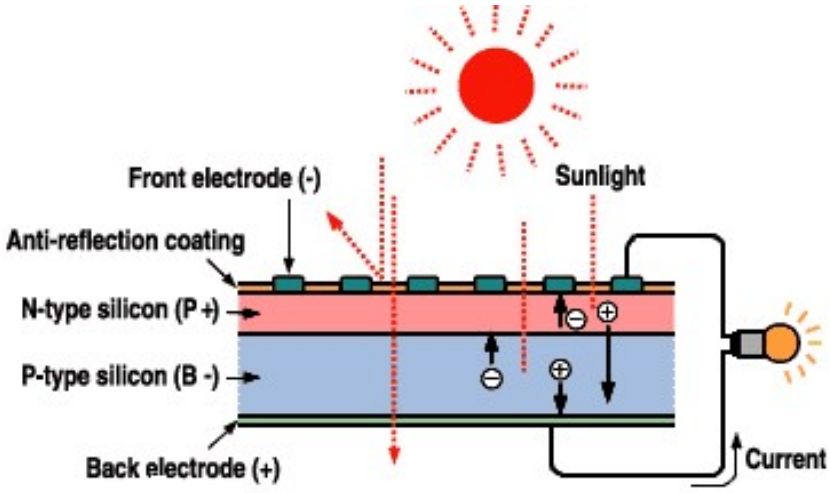

Fig. 2.1 The photovoltaic effect.

A typical crystalline-Si solar cell structure is shown in Fig. 2.2 [11]. The substrate is a p-type Si wafer with the resistivity of 1 Ω-cm. The thickness is ~180-200μm at the beginning and ~150μm after the process. The front surface is textured with random

pyramids to reduce reflection by increasing the chances of reflected light bouncing back into the Si surface. The n^+ emitter is formed by phosphorus diffusion with a thickness of about 0.5 μm. The doping concentration is controlled at a certain level to balance the resistive and recombination loss. A layer of silicon nitride (SiN_x) is deposited by PECVD serving as the anti-reflection coating (ARC). The thickness is around 75nm to maximize the absorption rate. Meanwhile, it contains hydrogen positive charges serving as a passivation layer. The front metal grid made of screen-printed Silver (Ag) is placed to contact the n^+ emitter. It is designed to be highly conductive and have low shading area. The backside electrode is screen-printed aluminum (Al) and goes through high-temperature firing. Part of the Al diffuses into Si and forms p^+ doped like alloy, called back surface field (BSF). The BSF is a barrier preventing minority carriers to diffuse to the backside contact.

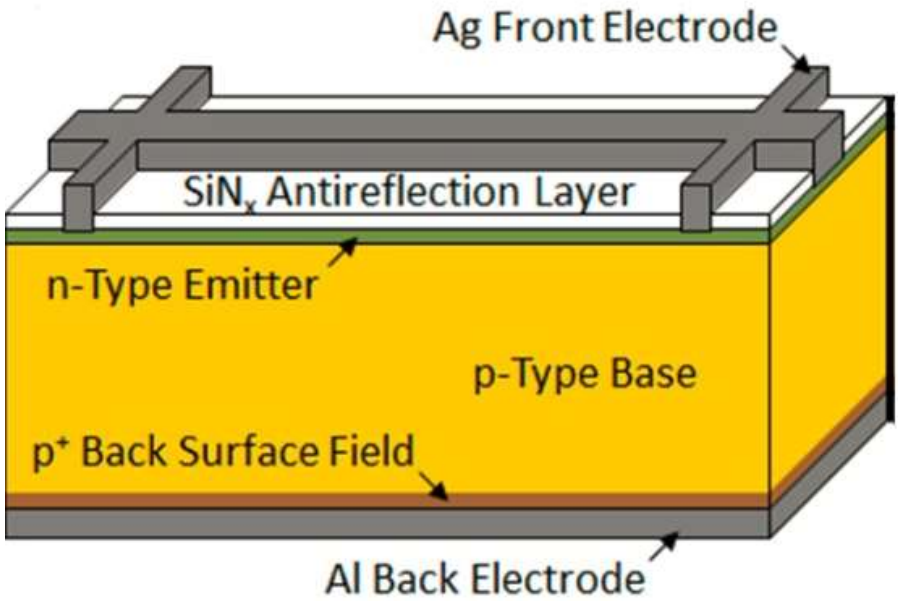

Fig. 2.2 Schematic of a crystalline-Si solar cell.

2.2 Operation Parameters

The solar cell is always characterized by a couple of parameters such as open-circuit voltage (V_{OC}), short-circuit current (I_{SC}), fill factor (FF), and cell efficiency (η), which are measured from current-voltage (IV) and power-voltage (PV) curves under illumination. The basic equation of an illuminated ideal solar cell is

$$I = I_L - I_0\left[\exp\left(\frac{qV}{nkT}\right) - 1\right] \tag{2.1}$$

I_L is the illumination current generated from light, I_0 is the reverse saturation current, n is the ideal factor of a diode. The IV and PV curves are shown in Fig. 2.3 [10].

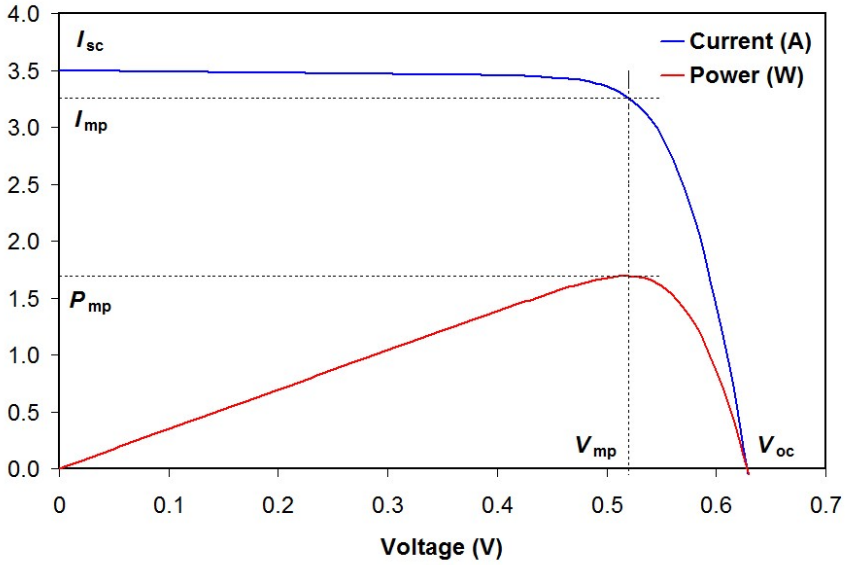

Fig. 2.3 Current-voltage (IV) and power-voltage (PV) curves

The open-circuit voltage (V_{OC}) is the voltage when no current flows out from a solar cell under illumination. The equation of V_{OC} derived from (2.1) is

$$V_{OC} = \frac{kT}{q}\ln\left(\frac{I_L}{I_0} + 1\right) \tag{2.2}$$

The V_{OC} is determined by the ratio of the illumination current and the reverse saturation current. While I_L is kind of stable for certain semiconductor material under constant illumination, I_0 varies by orders of magnitude due to the variation of surface and body recombination condition. Hence, the recombination in a solar cell is approximately evaluated by open-circuit voltage.

The short-circuit current (I_{SC}) is the current through the solar cell when zero voltage is applied to the device. The equation of I_{SC} derived from (2.1) is

$$I_{SC} = I_L - I_0 \tag{2.3}$$

Commonly, I_0 is several orders of magnitude less than I_L, so $I_{SC} \approx I_L$ on condition that a negligible series resistance is connected to the solar cell.

The fill factor (FF) is defined as the ratio of the maximum power of a solar cell to the product of V_{OC} and I_{SC}. The I_{mp} and V_{mp} are corresponding current and voltage when a solar cell is working at the maximum power point, which determines a square region in Fig. 2.3. The equation of FF is

$$FF = \frac{I_{mp}V_{mp}}{I_{SC}V_{OC}} \tag{2.4}$$

The FF is used to describe the ability of a solar cell to output power, indicating larger FF leads to greater power. Generally, the solar cell with a higher V_{OC} is possible to have a larger FF since the “square region” takes more portion of the IV curve.

The cell efficiency (η) is the percentage of maximum output power to input power, which is used to compare the performance of two solar cell. The equation of efficiency is

$$\eta = \frac{I_{mp}V_{mp}}{P_{in}} = \frac{I_{SC}V_{OC}FF}{P_{in}} \tag{2.5}$$

Since the input power density from the solar radiation onto the Earth's surface is ~100 mW/cm^2, the efficiency can be calculated from the above three parameters.

2.3 Loss Mechanism

In theory, a single p-n junction Si solar cell can achieve up to 29% efficiency considering its inherited limitations [12]. However, the world record high efficiency is reported to be ~25% in the lab [13]. In the commercial market, the common conversion efficiency of multi-Si solar cells is only ~18.0% while that of mono-Si solar cells is ~19.8% [14]. The efficiency drops further when the solar cells are packaged into a module. Various loss mechanisms lead to this result, including optical loss and electrical loss on the cell side and mismatch loss on the module side.

(1) Optical loss

The optical losses are shown in Fig. 2.4 [15]. The reflection loss is caused by the reflection of incident light from the solar cell front surface. The shading loss is because of the fingers preventing incident light to enter the cell. The incomplete absorption refers to the photons escaping from the substrate or being absorbed by the contact metal.

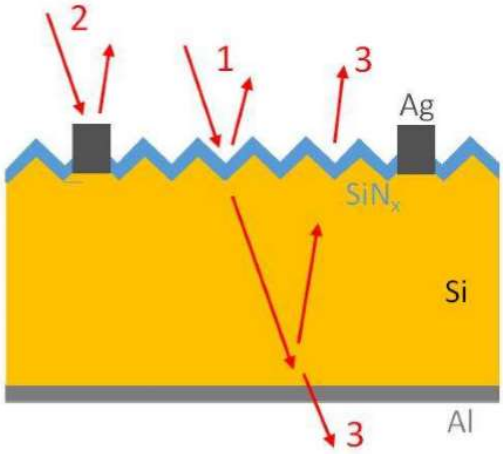

Fig. 2.4 Optical loss: (1) reflection loss (2) shading loss (3) incomplete absorption

The reflectivity of a flat silicon surface is about 36%. Texturing the surface helps to reduce it to less than 10% by increasing the probability of absorption due to multiple reflections. The reflected incident light bounces back among the surface pyramids and is re-absorbed by Si. Further, an appropriate dielectric layer placed on top of the textured surface reduces the reflectivity to about 5%. The thickness and the refractive index of this layer are calculated carefully to utilize the destructive interference of waves to prevent the light to escape.

The energy is extracted from the contacts on both side and shading loss comes from the front side contact. In the current commercial solar cells, the contact shading is around 3-6% of the front area. In this case, the front electrode grid can be improved by narrowing contact fingers to reduce the shading loss. However, it is limited by the contact metal resistivity and the front metallization method due to resistive loss. Another method is placing both contacts on the rear side called interdigitated back contact (IBC) solar cell, achieving 25% efficiency by SunPower [16]. This method requires the substrate has a relative long minority carrier lifetime, usually carried out in n-type wafers.

The incomplete absorption refers to the photons escaping from the Si or being absorbed by the electrodes. Incident light with a long wavelength is not absorbed within the thickness of Si body. It is improved by refining the back side and reflecting the light back to the cell. On the rear surface of most wafer-Si solar cells, the metal electrode, typically Al, can serve as a reflector. It is better to have a flat back surface to reduce the surface recombination.

(2) Electrical loss

The electrical loss is divided into recombination loss and resistive loss. The recombination loss is inside of the cell, as the electrons and holes recombine before they are extracted out. As shown in Fig. 2.5 [17], the mechanism includes **radiative recombination**, **SRH recombination**, and **Auger recombination** in the body, and **surface recombination** via surface states. Radiative recombination is a direct band-to-band recombination between an electron and a hole. As Si is an indirect semiconductor, it is negligible because few phonons assist this process. Auger recombination happens when the energy produced by electron and hole recombination is absorbed by a second electron or hole in the same energy level, then is emitted to the lattice structure. It is dominant in when the carrier concentration is high as in n^+ emitter but not the p-type substrate. SRH recombination, analytically described by Shockley, Read and Hall, refers to the recombination assisted by impurities or dislocation states in the forbidden bandgap in the semiconductor. It is the main recombination process in typical multi- and mono-crystalline Si material, as the impurities are the dopant in the substrate. Surface recombination is an extension of SRH recombination as there is a high density of defects due to the abrupt ending of the crystal lattice at the surface. It can be improved by passivating the surface with a mending method to reduce the dangling bonds, or with a field effect method to reduce the density of minority carrier concentration.

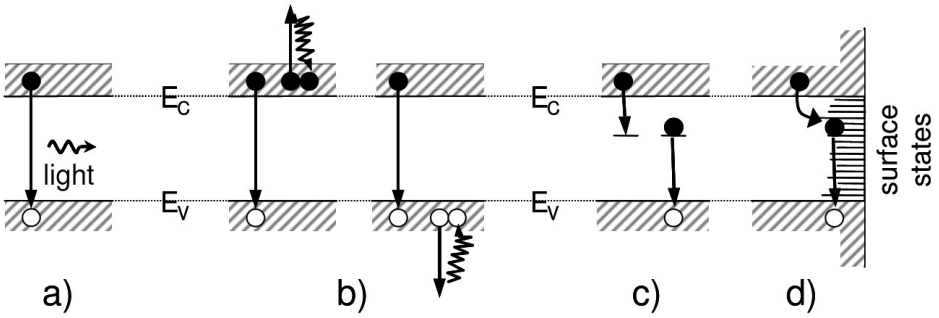

Fig. 2.5 Recombination mechanisms (a) Radiative (b) Auger (c) SRH (d) surface

The resistive loss comes from the parasitic resistances to the ideal solar cell, including series resistance and shunt resistance. The equivalent circuit for a real solar cell is shown in Fig. 2.6 [10].

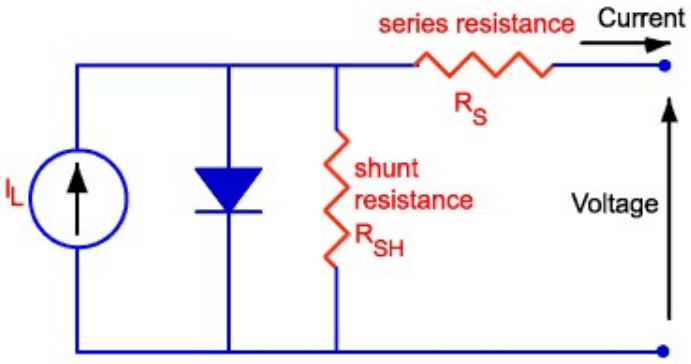

Fig. 2.6 Equivalent circuit of solar cell

Considering both series and shunt resistances, the equation for a solar cell becomes

$$I = I_L - I_0 \left\{ \exp\left[\frac{q(V + IR_S)}{nkT} \right] - 1 \right\} - \frac{V + IR_S}{R_{SH}} \tag{2.6}$$

The series resistance is caused by 1) the current flow through the emitter and base of the solar cell, 2) the contact resistance between cell material and metal contacts, and 3) the current flow through the front metal contacts including busbar and fingers. It consumes much power from solar cells working at high current densities and takes up a portion of power loss. The shunt resistance comes from manufacturing defects providing a leakage current path. It is especially severe and conspicuous for a solar cell under low illumination when the light current is small. Both parasitic resistances lower the conversion efficiency of a solar cell by reducing the fill factor as shown in Fig. 2.7 [10].

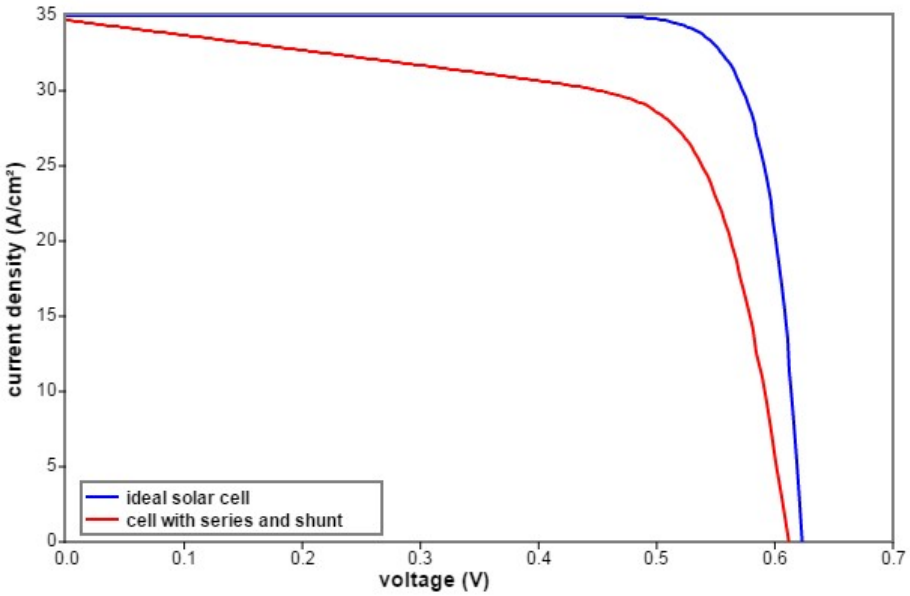

Fig. 2.7 Compare of ideal and non-ideal solar cell

(3) Mismatch loss

It is always a goal for manufacturers to produce high-performance solar cells. However, a stand-alone well-made solar cell is not enough to the photovoltaic industry. Individual solar cells are connected and encapsulated into a module, and then utilized to build a solar farm or rooftop PV stations. In this case, mismatch effect is an unavoidable significant factor to be considered when designing a PV module.

Since solar cells are cascade-connected to each other in a PV module, where series mismatches are the most common type of mismatch encountered. As shown in Fig. 2.8 [10], when two solar cells are series connected, the current flowing through one cell is equal to that of the other one, and the total voltage is the sum of both working voltages. If they have different illumination currents, the small one sets a limitation for the cascade system and cannot make full use of the output power capability.

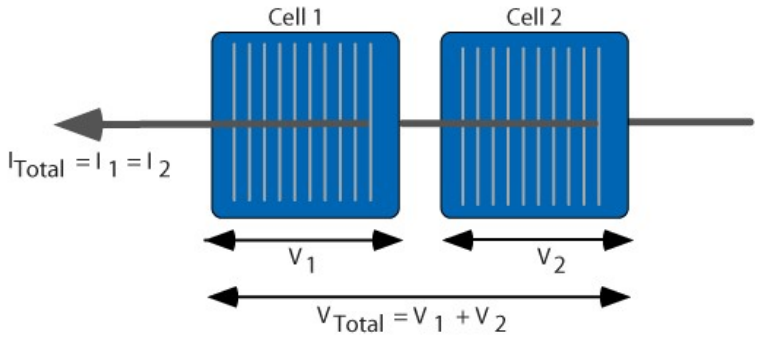

Fig. 2.8 Two solar cells connected in series

The parallel mismatch is not an issue for series connected solar cells within the same module, but it is a common problem for modules parallel connected in large arrays. The module level mismatch could be briefly explained by parallel connected solar cells, as shown in Fig. 2.9 [10]. Both solar cells share the same working voltage while their currents are added up to form the total current. In this case, one solar cell with lower V_{mp} determines the final voltage and prevents maximizing the other one's efficiency.

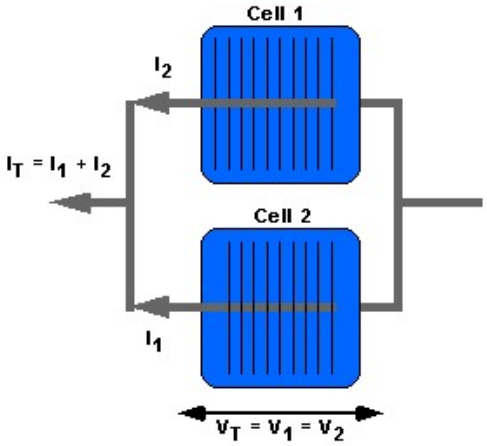

Fig. 2.9 Two solar cells connected in parallel

3. SOLAR CELL MANUFACTURING PROCESS

In photovoltaic industry, mono- or multi-crystalline Si solar cells are manufactured in mass production. Fig. 3.1 shows the typical production flow from Si wafers to final solar cells.

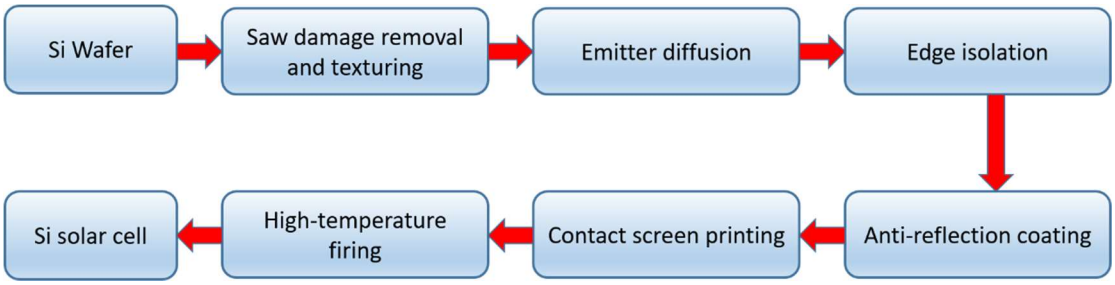

Fig. 3.1 Production flow of industrial Si solar cells

3.1 Saw Damage Removal and Texturing

The Si wafers in solar cell fabrication are sliced from solar-grade Si ingots into ~200μm thick wafers by slurry or diamond wire saw, so it is inevitable to leave saw damages and contaminations on the surface. Sodium hydroxide (NaOH) or potassium hydroxide (KOH) based solution is commonly used to remove the damages. The reaction is

$$NaOH + Si + H_2O \rightarrow Na_2SiO_3 + H_2 \quad (3.1)$$

The wafers are put in hot the alkaline-based solutions with ~8 wt% and the first ~10 μm surface layer is etched off, ensuring the surface is clean.

Texturing is forming a “rough” surface to increase the chance of light being absorbed by Si. For mono-crystalline Si, diluted NaOH or KOH with isopropyl alcohol (IPA) or other additives is used to texture the surface. The reaction is the same as saw damage removal but the composition of the solution is different. Selective etching happens for the Si of <100> orientation and forms pyramidal structures with the size of several micrometers, as shown in Fig. 3.2 [18].

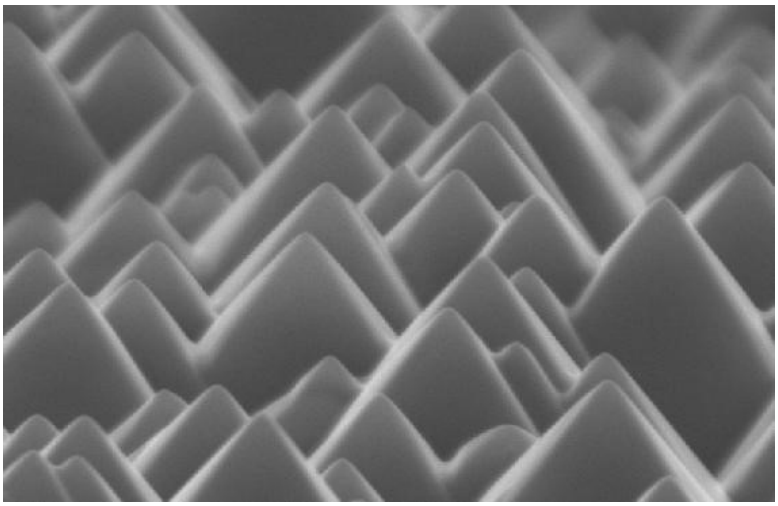

Fig. 3.2 Morphology of textured mono-crystalline Si surface

Multi-Si have various oriented crystal orientations on the surface, so the method described above is not suitable. A mixture of fluoric acid and nitric acid (HF/HNO_3) is used to texture the multi-Si. The reaction is

$$Si + HNO_3 + HF \rightarrow H_2SiF_6 + H_2O + NO_2 \quad (3.2)$$

The HNO3 oxidizes the Si surface and the HF etches off the oxide, leaving a textured surface, as shown in Fig. 3.3 [19].

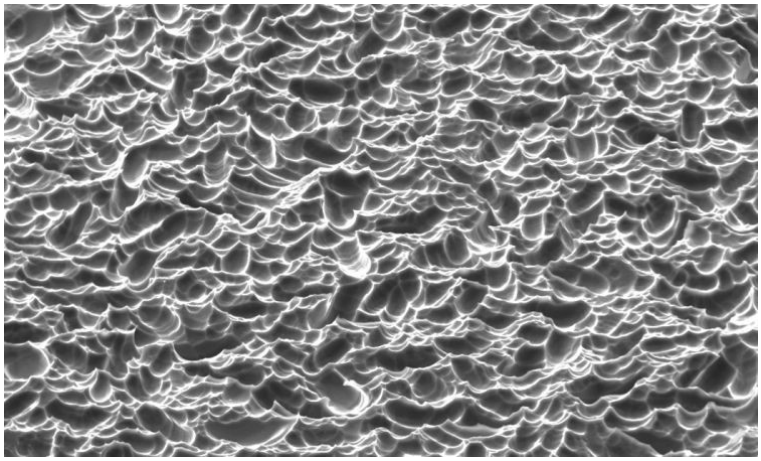

Fig. 3.3 Morphology of textured multi-crystalline Si surface

In recent years, texturing Si surface with reactive ion etching (RIE) or nanoparticle-catalyzed etching to form nanowires on the surface called “black silicon” technology was introduced to further increase the absorption efficiency [20-23].

3.2 Emitter Diffusion

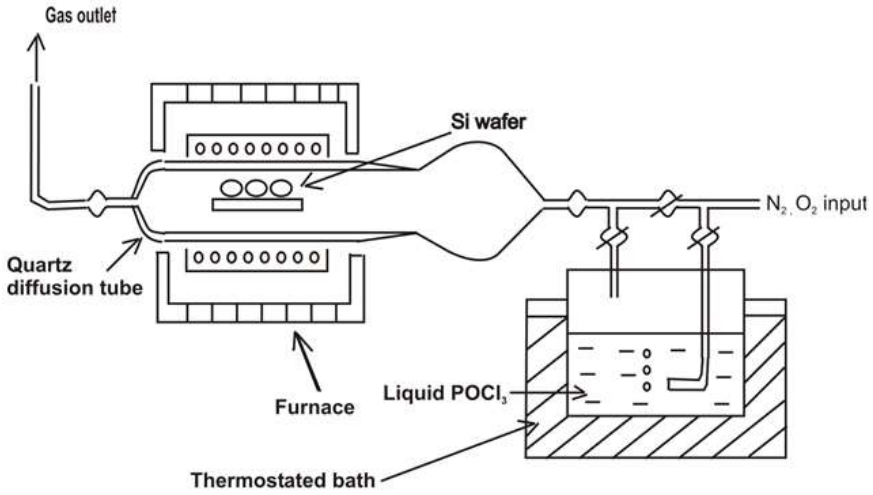

Fig. 3.4 Schematic process of $POCl_3$ diffusion in a doping furnace

The emitter diffusion process is to form the p-n junction on the Si wafers. The doping profile is critical to the final efficiency. For one thing, the emitter surface should be highly doped to form an Ohmic contact with finger electrodes. For the other thing, the amount of dopant reflected by the sheet resistance is required to be carefully controlled to balance the emitter recombination and the lateral carrier diffusion. This is the only long-time high-temperature up to 900ºC process in the fabrication usually carried out in doping furnace. Most of the Si solar cells are p-type and need a n^+ emitter formed by phosphorous (P) diffusion. Liquid state phosphorus oxychloride ($POCl_3$) is the common source of P. As the process shown in Fig. 3.4 [24], carrier gas nitrogen (N_2) and reaction gas oxygen (O_2) flow through liquid $POCl_3$ and bring it into the furnace. $POCl_3$ reacts with O_2 leaving solid P_2O_5 on the wafer surface, then P_2O_5 further reacts with Si to generate P. With the high temperature, P diffuses into Si surface and forms p-n junction. The reactions are

$$POCl_3 + O_2 \rightarrow P_2O_5 + Cl_2 \tag{3.3}$$

$$P_2O_5 + Si \rightarrow P + SiO_2 \tag{3.4}$$

A layer of phosphosilicate glass (PSG) is generated on the surface during the process. It is removed by HF before anti-reflection coating (ARC). For n-type Si substrates demanding a p+ emitter, boron tribromide (BBr3) serves as the doping source and the process is similar to P diffusion.

3.3 Edge Isolation

Fig. 3.5 Back and edge etching of Si wafer

After $POCl_3$ diffusion, the wafer is doped all around, thus the edge isolation is required prevent the emitter shunting to the body. One way to achieve edge isolation is plasma etching. The batch of doped wafers is stacked on top of each other and go through the plasma CF_4 and O_2. It etches off the edges but leaving both sides doped with P. The extra doped P is compensated in the follow-up process. In the current industrial process, wet etching is employed for edge isolation [25, 26]. The process also applies the HF/HNO_3 etching method but only allows the downside of the wafers touching the acid and protects the upside with water mask, as shown in Fig. 3.5 [27].

The advantage of the wet etching is that it can be integrated with PSG removal in an inline process. As shown in Fig. 3.6, the edge isolation is adjusted ahead to utilize the HF in PSG removal for native oxide cleaning. They are always carried out in the same equipment and considered to be one step process.

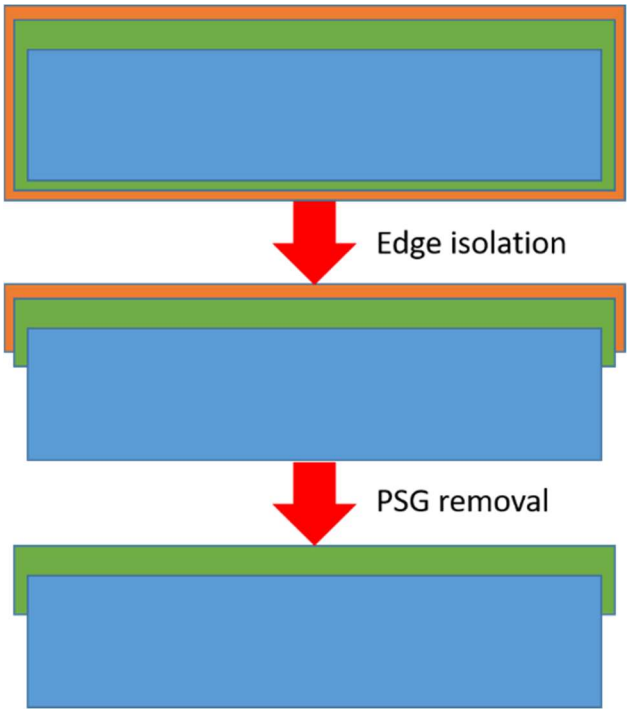

Fig. 3.6 Schematic process of PSG removal and edge isolation

3.4 Anti-Reflection Coating

The textured front side of Si solar cell is covered with an anti-reflection coating (ARC) layer. For n^+ emitter, it is usually plasma-enhanced deposited (PECVD) SiN_x. The ARC layer has two roles. First, it helps increase the absorption of light. The thickness of the ARC layer is calculated per the refractive index of Si and SiN_x as well as the energy reflected light if the thickness $d_1=\lambda_0/4n_1$, as shown in Fig. 3.7 [10]. Meanwhile, reflection is further reduced if $n_1=\sqrt{n_0 n_2}$, so the best n1=2 as n0=1 for air and n2=4 for Si. The

optimized thickness is calculated ~75nm with the appearance color blue as the strongest spectral irradiance is with the range of visible wavelength (390-700nm).

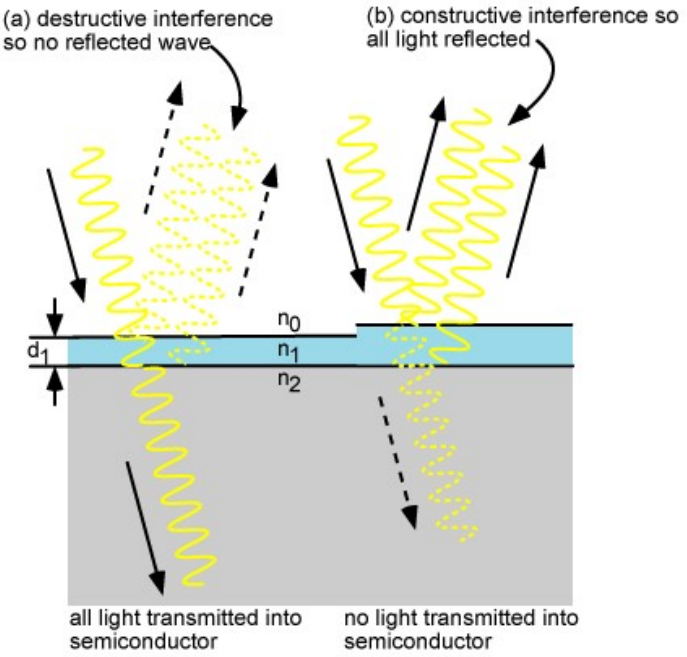

Fig. 3.7 Schematic of interference (a) destructive, (b) constructive

The second role is the passivation of Si surface. The PECVD SiN_x contains a large amount of H as positive charges, which help prevent the diffusion and recombination of holes in the emitter. To enhance the passivation effect, multi-layer ARC like SiO_2/SiN_x is employed in solar cell fabrication. For p^+ emitter on an n-type substrate, SiNx by PECVD is not suitable as negative charges are required. Al_2O_3 deposited by atomic layer deposition (ALD) is used for passivation. Since the deposition rate of ALD is too slow, an additional layer is stacked to adjust the reflection.

3.5 Contact Screen Printing and High-Temperature Firing

The contacts on both sides of Si solar cells are formed by screen printing. It is a simple and fast process in-room environment. The metal paste is squeezed through a blocking

stencil onto the solar cell, as shown in Fig. 3.8 [17]. The stencil is patterned for the front side and blank for the backside. For the front side, there are difficulties in applying screen printing. First, the frontside contact must be as narrow as possible to have little shading, so the metal is required to be highly conductive. Second, the frontside Si is covered with SiN_x with no exposure to metal, so it is required to bridge them and form an Ohmic contact. Ag paste is used for frontside screen printing. There are around no less than 80% Ag in it with glass frit as the rest. The applied Ag paste burns through the SiN_x layer during the follow-up high-temperature firing and forms contact with Si. The resolution of screen printing is ~8μm, much wider than lithography method. In recent years, fine line double printing (FLDP) was introduced to increase the aspect ratio and narrow down the front contact fingers [28, 29]. Additional alignment is required for this advanced technique.

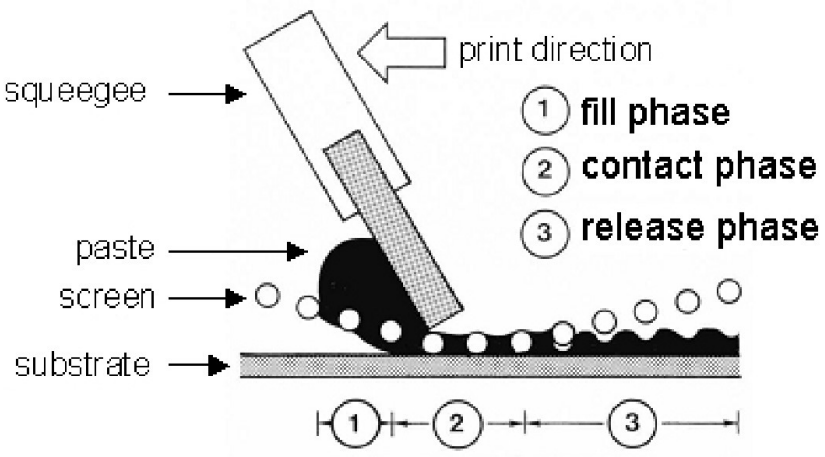

Fig. 3.8 Process of screen printing

Traditionally the backside process is simpler. The whole area is printed with a layer of Al paste and then goes through firing. The Al-Si alloy is formed producing a p^+ doping like back surface field (BSF). An additional print of Ag pads is required for soldering. The popular PERC structure solar cell is more complicated as the backside is patterned and

passivated before screen printing [30-33]. Only one-step firing is needed for both sides screen printing, as the pastes are adjusted to use the same firing temperature up to 950ºC. The firing is usually carried out in a belt furnace with different temperature zones.

4. ELECTROPLATED ALUMINUM FRONT ELECTRODE SOLAR CELL

4.1 Introduction

Al is a widely used metal in the semiconductor industry. In the early years, Al metallization was the standard process in MOSFET fabrication as the contacts and interconnection wires [34, 35]. Al is a chemically stable material and compatible with Si, i.e. Al can be directly deposited on Si surface without harming the performance of Si. This is a significant advantage over many other common high-conductive metals like Ag, Cu, and Au. These metals are active and always treated as contaminations if any of their ions are diffused into the Si body. The electrons and holes recombine with the assistant of these impurities so the Fermi level is changed and the p-type or n-type Si is not functional. Al, on the contrary, has a very low solubility in Si and vice versa [36-38]. They form Al-Si alloy during the metallization process and no Al ions diffuse into Si. Though Al and Si have different values of work function which could lead to Schottky contact, they are able to form Ohmic contact if Si is heavily doped. In the photovoltaic industry, the Al is used as the backside electrode by screen printing, as mentioned in Chapter 3. The reliability is approved by the long-term application and research with the development of Si solar cells [13, 39].

Although Al is always a cheap and reliable metal candidate for Si solar cell front side metallization, an economic and convenient method is required for fabrication in production. There are different processes available for the Al metallization. In the semiconductor industry, Al is usually deposited by thermal evaporation or sputtering. As they can achieve fine lines with less shading on the front side [40], it is not suitable for solar cell production. For one thing, the deposition rate is very slow at 1~2 nm/s while the thickness of the front

electrode is at least 15~20 um, so it is hard to support volume production in demand. For the other thing, the deposition is not self-aligned as the whole area is covered with the metal after the process. Lithography or other processes are required to achieve patterning, which further increases the fabrication complexity and cost on top of the vacuum-based process. Screen-printing is the metallization method currently used in the photovoltaic industry to deposit Ag on the front side and Al on the back side. While Ag screen-printing prevails, there is no open reported result on Al screen-printing for the front electrode [41]. The first issue is the molten temperature of Al is only ~600 ºC, thus the aspect ratio cannot be kept during the ~900ºC high-temperature firing. The second issue is the resistivity of Al paste is too high for the front electrode. Even the resistivity of Ag paste is ~5 times of pure Ag, it is not acceptable if Al paste has the same resistivity ratio. As of now, Al screen printing has no clear potential for the application in Si solar cell manufacturing. Hence, a new room-temperature solution-based metallization method is desired in the development of electroplating of Al as the front electrode of Si Solar cells.

In recent years, the research on electroplating of Al in an ionic liquid is heated up for anti-corrosive coating on metals[42-45]. Since this kind of room temperature electroplating is a simple and cost-saving process, it has the potential to be used in solar cell fabrication. Our lab first introduced and proved it can be used for Si solar cell fabrication as well [46-49]. In this chapter, section 4.2 explained the background and the theory of Al electroplating in an ionic liquid. Section 4.3 reported the results on the Si solar cell with electroplating of Al as the front electrode. The deposited Al is dense and continuous and the fabricated cells have a decent efficiency compared to Ag electrode solar cells. Section

4.4 introduced a modified cell structure which is spiking-resistant and reliable compared to traditional structure solar cells.

4.2 Theory of Al Electroplating in Ionic Liquid

Electroplating of Al requires a non-aqueous solution because of its high reactivity potential (-1.67 V vs. NHE), or hydrogen(H) ions are reduced before Al ions and thus only H_2 is generated. The electroplating is usually carried out in inorganic molten salts [50] or organic solvents [51, 52]. Molten salts required an extremely high temperature up to 1000ºC, which is not acceptable in the solar cell fabrication (Firing process is also ~900 ºC but it is rapid thermal annealing in a short time). Organic solvents are commercially available for room temperature electroplating. However, safety issues are raised as they are volatile and flammable. In this case, we turned to the ionic liquid as the possible solution to the metallization for Si solar cell.

The ionic liquid is also a molten salt which contains only ions in it, but it is specific to certain materials with near room temperature melting points. There are many good properties in the ionic liquid [53]: (1) Serving as the solvent for a wide range of both organic and inorganic materials, (2) Potential to be highly polar but noncoordinating solvents due to poorly coordinating ions composition, (3) Providing a non-aqueous, polar alternative for two-phase systems with the immiscibility to different organic solvents, (4) Nonvolatility suitable for high-vacuum system without containment issues.

Most reported ionic liquids for Al electroplating are based on the mixture of anhydrous aluminum chloride (AlCl3) with 1-ethyl-3-methylimidazolium chloride (EMIC), 1-butyl-

3-methylimidazolium chloride (BMIC) and tetraalkylammonium halides [54-56]. The combination of $AlCl_3$ with these chloride salts are described below:

$$AlCl_3 + Cl^- \rightarrow AlCl_4^- + x(Al_2Cl_7^-) + y(Cl^-) \quad (4.1)$$

$$AlCl_4^- \leftrightarrow Al_2Cl_7^- + Cl^- \quad (4.2)$$

The composition of $Al_2Cl_7^-$ and Cl^- determines the property of the ionic liquid. Cl^- shows Lewis basic while $Al_2Cl_7^-$ shows Lewis acidic. The Lewis acidity/basicity is adjustable by adding $AlCl_3$ or [X]Cl into the solution. As for Al electroplating, the electrolyte is required to be Lewis acidic and the Al is reduced by the reaction:

$$4Al_2Cl_7^- + 3e^- \leftrightarrow Al + 7AlCl_4^- \quad (4.3)$$

When a negative potential is applied to the substrate, the electrons are accumulated to the surface and transferred to the electrolyte. With the assistance of the stable ionic liquid cations, the electrons are captured by the $Al_2Cl_7^-$ and Al is formed on the substrate surface, as shown in Fig. 4.1.

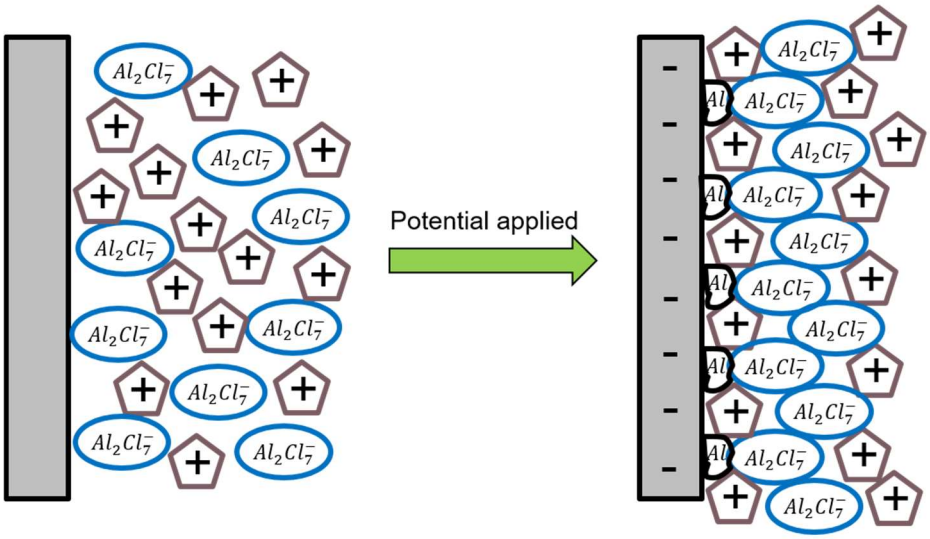

Fig. 4.1 Schematic of the Al electroplating theory

Though the ionic liquid is stable and nonvolatile at room temperature, it is sensitive to water as well as moisture. For one thing, the anhydrous $AlCl_3$ is reactive to H_2O. The moisture is absorbed by the $AlCl_3$ during the preparation of the ionic liquid and generate HCl. For the other thing, $Al_2Cl_7^-$ and $AlCl_4^-$ are also reactive to H_2O. The reaction generates Al-O-Cl compounds species and HCl [53]:

$$Al_2Cl_7^- + H_2O \rightarrow Al_2Cl_5O^- + 2HCl \qquad (4.4)$$

Since it is impossible to totally remove the ubiquitous moisture in the experiment environment, the process should be carefully controlled to prevent the OH- impurities trapped in the ionic liquid. One solution is to carry out the experiment in a vacuum system which is isolated from outside, but the cost is unavoidably increased. Another solution is to perform the experiment under inert gas protection which is much cheaper. Our lab also proposed a method that preheating the electrolyte above 100ºC to exclude the H2O liquid and diffuse the moisture with N2 gas. The resistivity of deposited Al has lower resistivity compared to that without preheating [47]. It is still under discussion the path to commercializing the ionic liquid electroplating and we are on the way to explore the unclear future application.

4.3 Al Front Electrode Si Solar Cell

As the electroplating of Al on Si was developed and carried out in our lab before, a Si solar cell with Al front electrode is also produced [48]. The fabrication of this solar cell is supported by Hareon Solar, who provided half-processed commercial Si solar cell substrates. The front grid patterning and electrode metallization are finished in our lab. The detailed experimental process and results are presented and discussed below.

4.3.1 Experimental

The ionic liquid was prepared by adding anhydrous $AlCl_3$ powders (99%, Aldrich) to 1-Ethyl-3-methylimidazolium Tetrachloroaluminate ((EMIm)$AlCl_4$) (≥95%, Aldrich) in a 100mL beaker on a hot plate within a nitrogen box to prevent moisture. The molar ratio between $AlCl_3$ and (EMIm)$AlCl_4$ was 0.5 to keep it Lewis acidic for Al electroplating. The solution was continuously stirred and heated at 120ºC for 1 hour to dissolve all the $AlCl_3$ powers and drive out possible moisture trapped in it. Then the temperature was lowered to ~80ºC as this was the optimized temperature for the Al electroplating in our lab. The color of the ionic liquid was yellowish at the beginning and turned to brown as more anhydrous $AlCl_3$ was added.

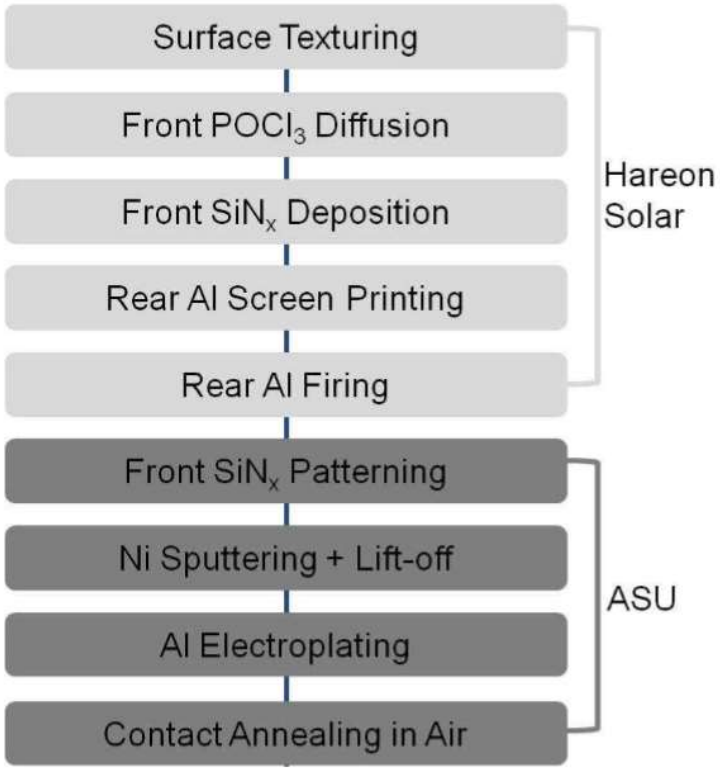

Fig. 4.2 process flow in Hareon Solar and our lab

Process flow shows in Fig. 4.2 [48]. The partially-processed crystalline Si solar cells from Hareon Solar shared the most common p-type cell structure with a front SiN_x coating, an n^+ front emitter, a p^+ back-surface field and a screen-printed Al back electrode. The cell fabrication started with a 12.5×12.5 cm^2, p-type, CZ Si(100) wafer. The wafer was textured to generate random pyramids on it and then doped with phosphorus to form the n^+ emitter with a sheet resistance of 90±5 Ω/sq. After the removal of phosphosilicate glass(PSG), a layer of SiN_x was deposited on the front side by PECVD to form the antireflection coating (ARC). Subsequently, the backside Al electrode was screen printed and then the wafer went through a firing step at ~750˚C, which formed the p+ back-surface field.

The industrial-size cells were cut into small cells of 3.75×5 cm^2. The active area of the all-Al cells was confined to 2.54×2.54 cm^2 (1×1 $inch^2$). The front side pattern design for the 1-inch cell area is shown in Fig. 4.3 [15]. Two contact regions were designed at the long side of the sample to connect with the electrode. Photolithography was used to pattern the SiN_x layer. A positive photoresist was applied by spin-coating and exposed under a photomask. After development, the SiN_x within the opening was etched off by HF. A layer of Ni (100-300 nm) was then deposited by sputtering over the remaining photoresist as well as the Si in the opening. After dipping the cell into acetone in an ultrasonic bath, the photoresist and the Ni on it were removed, leaving a Ni pattern in the opening ready for electroplating. An alternative and effective method for patterning is laser ablation followed by light induced or electroless Ni plating, but unfortunately, we have no such capabilities. This Ni seed layer is to assist Al electroplating due to the poor and non-uniform adhesion between direct electroplated Al and highly resistive Si (>1 Ω-cm). Electroplated Al fingers on the Ni seed layers were proven to be adherent and dense.

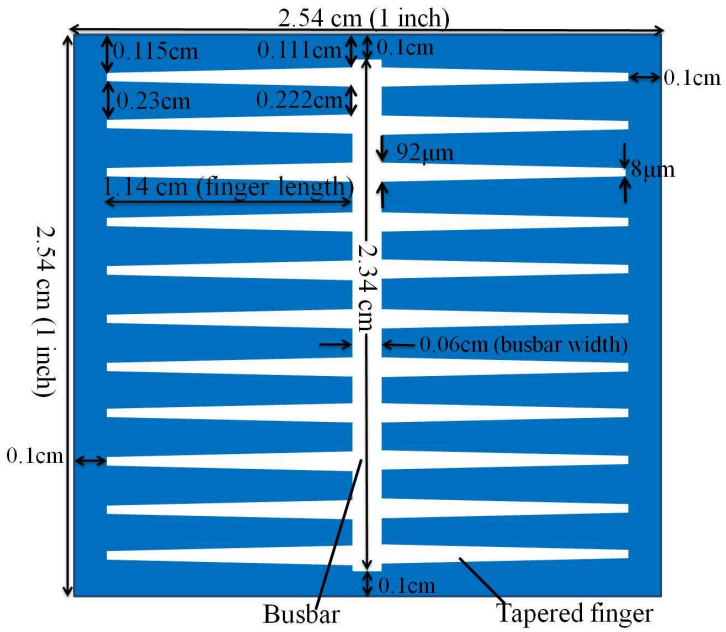

Fig. 4.3 A sketch of the final grid design

The electroplating employed a three-electrode electrochemical method to deposit Al. The sacrificial counter and reference electrodes used 99.99% pure Al wires. The Al wires were cleaned in diluted hydrochloric acid (HCl) for 1 minute, followed by a deionized (DI) water rinse. They were transferred to the nitrogen box after blown dry. The sample was placed at the working electrode. It also required an HCl clean to remove the Ni surface oxide before electroplating. It is important to make sure no water or liquid is left on the sample and Al wires. During electroplating, the backside of the Si cell was covered with a Teflon sheet to restrict Al deposition to only the front Ni seed layer. The electroplating current was controlled at ~15 mA/cm2 at ~80ºC. The thickness of the resultant Al layer is ~25 µm. A final annealing was performed in a rapid thermal processing furnace in air at temperatures ranging from 150˚C to 400˚C for 1 min to imitate the required Ni-silicide process employed in most electroplated electrode solar cells. The finished sample went

through the efficiency test before and after annealing. Electroluminescence(EL) was also performed to characterize the quality of the solar cell.

4.3.2 Results and Discussion

Fig. 4.4 shows the photo of the fabricated Si solar cell with electroplated Al front electrode. The continuous and dense deposited Al is self-aligned to the pattern. There are sparse Al dots on the SiNx area, which is because the defects in SiNx passivation layer allow the Si below it plated with Al. If the quality of the SiNx is very poor, the uncountable plated dots will have a large shading on the front side. It is a common issue in electroplated solar cells called “ghost plating”. In our sample, this is not a big issue as the measured efficiency is not affected.

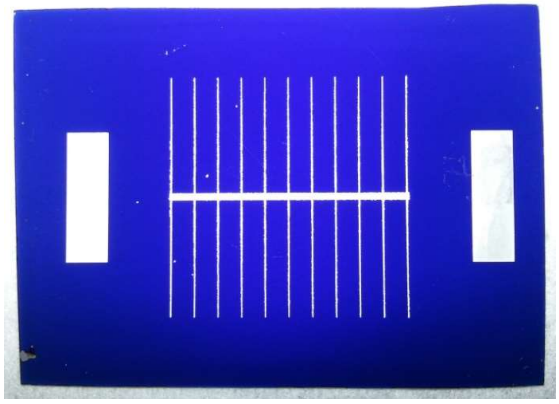

Fig. 4.4 Fabricated solar cell with All-Al electrode

Electroluminescence(EL) is a phenomenon that the semiconductor emits light in response to the passage of an electric current or to a strong electric field. When applying a forward current close to Isc to the Si Solar cell, the introduced electrons and holes recombine near the junction and cause light emission, which can be captured by an external detector. Since it is simple and fast, EL becomes a standard test in photovoltaic industry to characterize the quality of solar cells and panels. Fig. 4.5 shows the EL image the fabricated

solar cells with different efficiencies. The Higher efficiency solar cell has a brighter surface than the lower efficiency one, which verifies the EL test is effective to distinguish the solar cell quality. In the best-obtained sample, there are three dark lines crossing the fingers which are caused by possible damages or scratches during processing. The dim area between fingers shows the sheet resistance is kind of large with the current spacing distance.

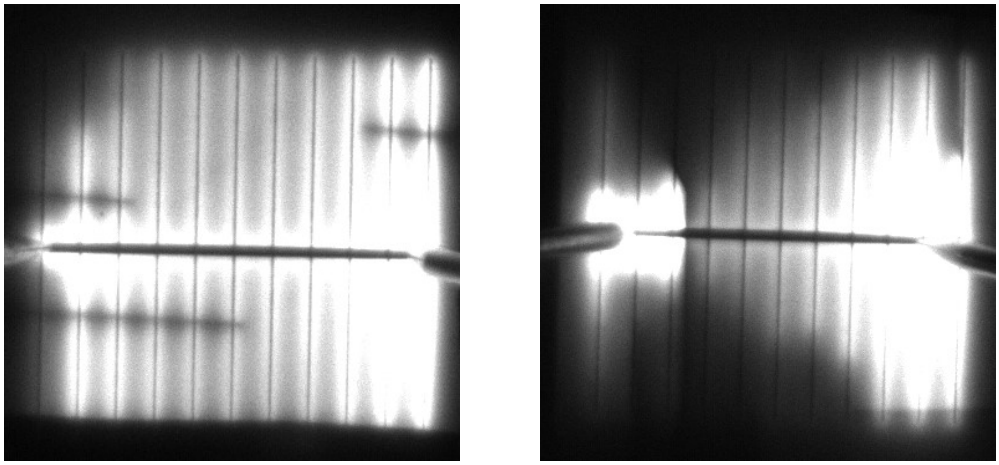

(a) (b)

Fig. 4.5 EL image of the all-Al Si solar cell with the efficiency (a) 14.7%, (b) 12.8%

The efficiency was measured under standard one-sun condition (AM1.5G, 100 mW/cm^2, 25˚C). In Table 4.1, the typical parameters of the solar cell before and after annealing is extracted. The best annealing temperature happened at 200ºC giving 14.6% efficiency. The fill factor(FF) is only 64.6% with different annealing temperatures from 150˚C to 400˚C. Taking consideration of the EL test result, we believe both series and shunt resistances are not optimized for this cell. Using the initial efficiency as the baseline, the normalized efficiency (η/η_0) as a function of annealing temperature is plotted in Fig. 4.6. The efficiency increases and peaks at 200ºC, then it is reduced as the temperature keeps increasing. Since the reported optimized annealing temperature is 350~450˚C for the formation of Ni-Si, our record is contradicted with it. The possible reason is that part of the

Al broke through the Ni layer like spiking and diffused into the surface Si n^+ emitter, thus the PN junction was shunted, leading the efficiency drop. Though the performance of this cell is not perfect, it is still a working solar cell and demonstrates the potential of Al front electrode solar cell.

Table 4.1 One-sun parameters of an all-Al Si solar cell with three different annealing temperatures.

	Voc (mV)	Jsc (mA/cm2)	FF (%)	η (%)
No annealing	617	35.84	64.3	14.2
Annealed at 200˚C (best)	626	35.98	64.6	14.6
Annealed at 400˚C	601	35.56	50.9	10.7

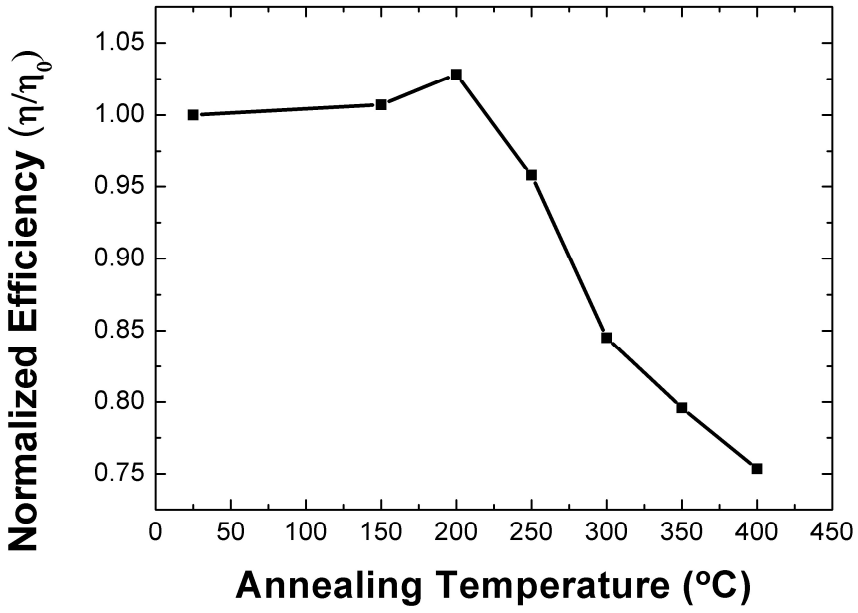

Fig. 4.6 Normalized efficiency of an all-Al p-type cell as a function of contact annealing temperature

4.3.3 Summary

In this section, a common structure p-type Si solar cell with an electroplated Al front electrode is demonstrated. The fabrication started with the commercial available partial processed p-type cells and finished the Al electroplating front electrode metallization in the lab. Though the finished solar cell's maximum 14.6% efficiency is relative low, it proved the feasibility to employ Al electroplating to replace Ag screen printing in the Si solar cell fabrication. The effect of annealing on the Al/Ni electrode is investigated at different temperatures. The efficiency reaches its peak at 200˚C and then decreases as the temperature rises due to possible Al spiking. EL test shows there is room to further optimize the pattern design and fabrication process.

4.4 Spiking Resistant Rear Junction Solar Cell

In our processing electroplated Al on a Ni barrier layer in p-type Si cells, high-temperature annealing at 350–450ºC is often required to improve the Ni/Si contact resistivity and adhesion [57]. However, significant shunting has been noticed after annealing [48, 58]. The shunting is attributed to spiking, which shunts the front p-n junction and results in a large leakage current. In order to minimize the effect of shunting, it may be necessary to keep the p-n junction away from the Al. Therefore, the rear junction cell structure is a natural choice to achieve a spiking-resistant all-Al cell.

In this section, we report a spiking-resistant all-Al rear-junction n-type Si solar cell. The cell is prepared by electroplating Al on an n-type cell with a fired Al back electrode as the rear junction. The finished cell is annealed in a rapid thermal annealing (RTA) furnace in air. The performance of the cell shows that this n-type rear-junction cell has excellent resistance to shunting and Al spiking compared with a p-type front-junction all-Al cell

under a similar process. When the n-type all-Al cell is compared to control cells with an Ag front electrode and fired Al rear junction produced in an industrial R&D line, it shows similar performance confirming the possibility of replacing Ag with Al.

4.4.1 Experimental

Fig. 4.7 shows the process flow to fabricate this all-Al n Si solar cell. The fabrication process was similar to the Section 4.3 but started with a 180 μm, 156×156 mm^2, n-type, CZ Si (100) wafer. The minority carrier lifetime in the starting wafer was larger than 1000 μs, which is required for a rear junction solar cell. The wafer was textured to generate random pyramids on it and then doped with phosphorus to form the n^+ front side field (FSF). The sheet resistance of the FSF was 80–90 Ω/□. After the removal of phosphosilicate glass(PSG), a layer of SiN_x was deposited on the front side by PECVD to form the antireflection coating (ARC). Before opening the front side contact area, screen printed Al was applied to the backside and fired at 950ºC. The firing created a heavily Al-doped p^+ layer and formed the rear p-n junction. All the above processes were performed in an industrial R&D line of Canadian Solar. Then the partially-processed n-type solar cells with a SiN_x ARC, an n^+ FSF layer, and a screen-printed Al rear junction were shipped to ASU. Canadian Solar also fully processed some of the cells with a screen-printed Ag front electrode for comparison.

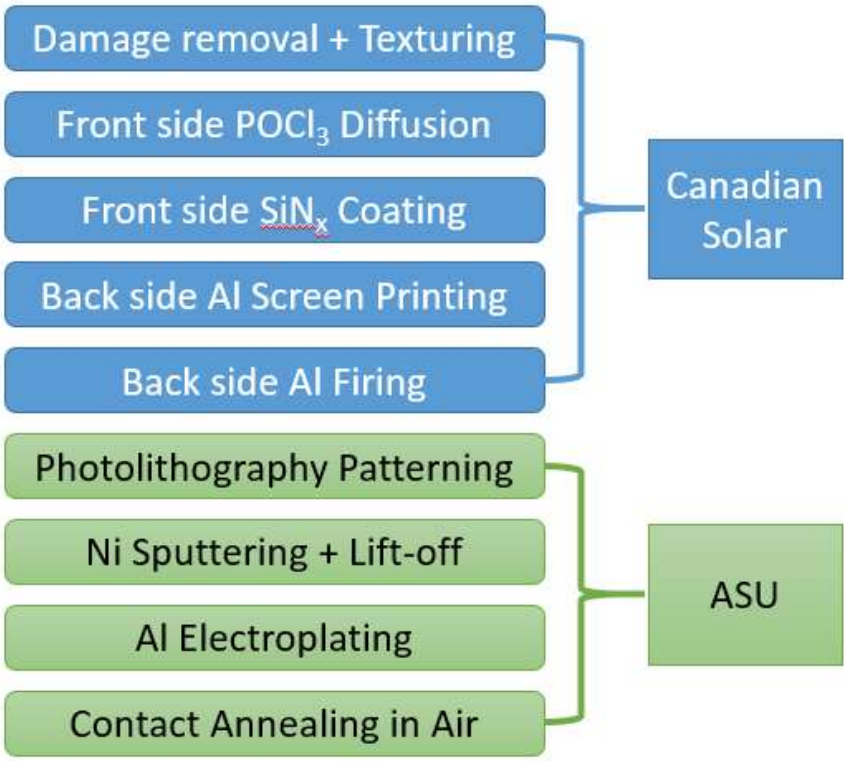

Fig. 4.7 Fabrication process flow for an all-Al n-type rear-junction crystalline-Si solar cell

The industrial-size cells were cut into small cells of 4×5 cm^2. The active area of the all-Al cells was confined to 2.54×2.54 cm^2 (1×1 $inch^2$). The subsequent process for sample preparation was the same as the Section 3.3. In the electroplating, a 50×50 mm^2 Al foil (≥99.99%, Alfa Aesar) was used to replace the Al wire as the sacrificial anode. The electroplating was processed at a constant current density of ~10 mA/cm^2 until the resultant average thickness is ~20 μm. After an initial efficiency test, the cell was annealed in an RTA furnace in air at temperatures from 150˚C to 450˚C for 1 min and the efficiency was measured at each temperature. The cross-section of this n-type cell compared to the p-type cell is schematically shown in Fig. 4.8.

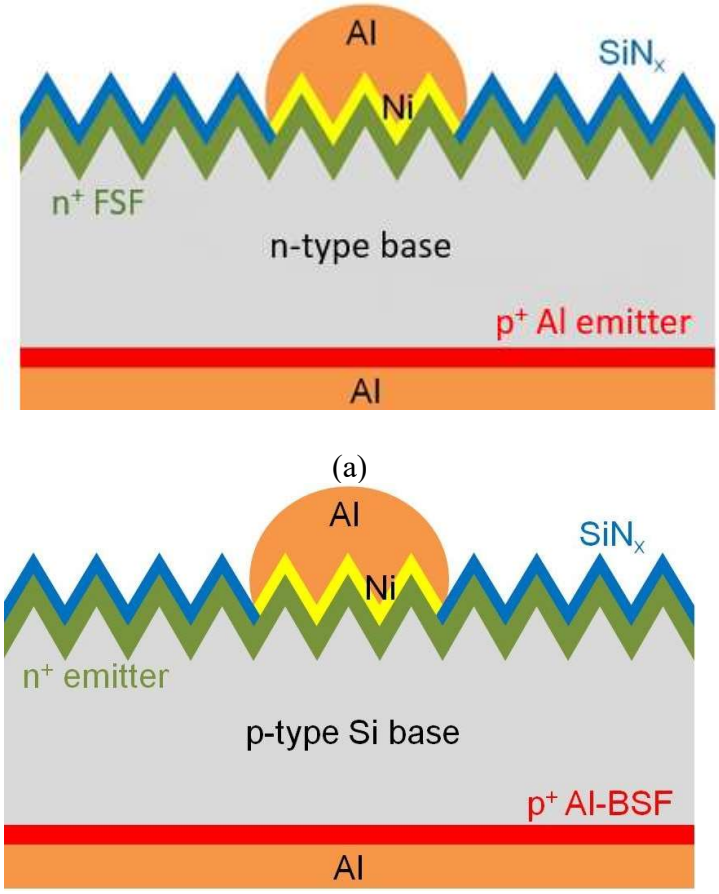

Fig. 4.8 Schematic cross-section of an all-Al Si solar cell (a) n-type, (b) p-type

4.4.2 Results and Discussion

The efficiency of the cell was measured in an ABET solar simulator under standard one sun conditions: AM 1.5G, 100 mW/cm^2, 25ºC. The effect of annealing in air at different temperatures from 150ºC to 450ºC was also investigated. Fig. 4.9 illustrates the efficiency of the cell at different annealing temperatures. The efficiency is 17.8 % at 150˚C and 250˚C. It increases slightly to 17.9% at 350˚C. Then it decreases gradually at higher temperatures and reaches 17.4% at 450˚C, indicating a 0.5% absolute degradation from the highest value.

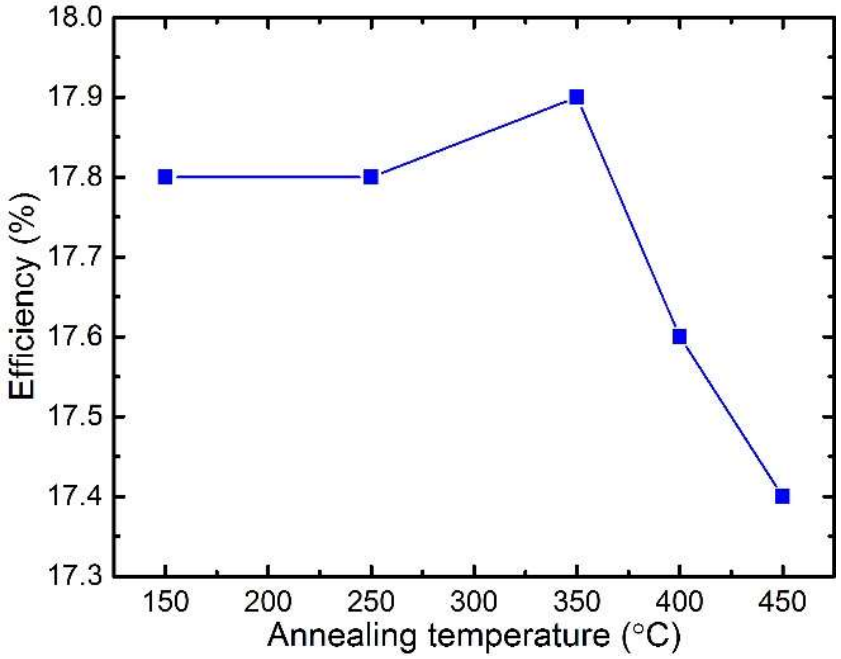

Fig. 4.9 Efficiency of an all-Al n-type rear junction Si cell as a function of annealing temperature.

The thermal behavior of this all-Al n-type cell is compared with a p-type all-Al cell fabricated under a similar process in Fig. 4.10. This p-type cell was reported in our previous paper[47]. For the p-type cell, its normalized efficiency of after 400˚C annealing decreases to ~75% of its initial efficiency. However, for the n-type cell, the normalized efficiency is larger than 97% after annealing at 450˚C. The result clearly confirms that the rear junction n-type cell is less susceptible to high-temperature annealing than the front junction p-type cell. Al spiking is suggested as the reason for the efficiency degradation in the p-type cell with an electroplated Al front electrode. Since the heavily doped front emitter is thin in typical p-type Si cells, high-temperature annealing and Al spiking can easily penetrate the surface into the base and short the junction. Unlike the p-type cell, the n-type cell has a thick n-region under the front Al electrode and Al spiking does not

penetrate the n region. It is thus resistant to Al spiking. In principle, this cell may withstand a temperature as high as the eutectic temperature of Al and Si, 577˚C.

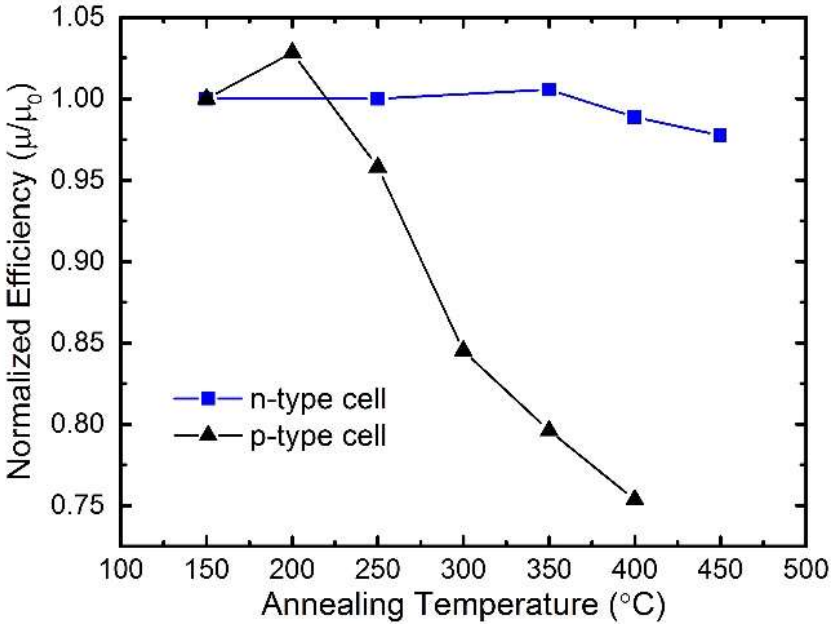

Fig. 4.10 Normalized efficiency of an all-Al p-type cell and an all-Al n-type cell as a function of annealing temperature.

Table 4.2 lists the detailed performance parameters of the n-type all-Al cell before and after annealing. The open circuit voltage (V_{oc}) decreases by ~3 mV. There are two reasons for the V_{oc} drop. First, the front side Al may penetrate the FSF and contact the lightly doped Si base. This reduces the separation between the quasi-Fermi levels across the p-n junction. Second, more defects and impurities may be introduced into Si through the edges during annealing. Both reasons lead to a higher reverse saturation current and thus the V_{oc} decreases. The consistent short-circuit current (J_{sc}) before and after annealing implies the quantum efficiency is stable and not deteriorated by spiking. This is an advantage of Al over Cu as Al has little effect on the minority carrier lifetime. The fill factor (FF) drops by 1.2% after annealing at 450ºC. This is attributed to an increased series resistance. The shunt resistance stays high at 3790 Ω-cm^2 and does not affect the FF, but the series resistance

slightly increases from 0.7 to 0.9 Ω-cm^2. Annealing shows no improvement in series resistance. The sputtered Ni is dense and of high quality. Our transfer line measurement (data not shown) reveals a contact resistivity of 2×10^{-4} Ω-cm^2 between Ni and Si. Annealing further improves the contact resistivity between Ni and Si. On the other hand, the oxidation of the front Al electrode in air may be the reason for the increase in series resistance, resulting in a lower fill factor.

Table 4.2 One-sun parameters of an all-Al n-type Si solar cell before and after Annealing

	Before annealing	Annealed at 450ºC
V_{oc} (V)	0.627	0.624
J_{sc} (mA/cm^2)	36.8	36.8
FF (%)	77.1	75.9
η (%)	17.8	17.4
R_s (Ω-cm^2)	0.7	0.9
R_{sh} (Ω-cm^2)	5070	3790

Table 4.3 lists the parameters of the all-Al n-type cell and a control cell with a screen-printed Ag front electrode. The control cell was processed in an industrial R&D line at Canadian Solar. The efficiency of the all-Al cell approaches 18%, just 0.3% absolute below the industrial cell with an Ag front electrode. Though further optimization is still necessary to improve the series resistance and fill factor of the n-type all-Al cell, Table 4. 3 confirms that electroplated Al is capable of replacing Ag as the front electrode in wafer-Si solar cells. It is also noticed that the V_{oc} of the all-Al n-type cell is lower than the control cell with an Ag front electrode. This is attributed to the fact that the two cells have different sizes and thus different perimeter/area ratios. Compared to the commercial 156×156 mm^2 cell, the

1×1 inch^2 small cell has a larger edge effect, thus the peripheral defects and impurities play a more important role as recombination centers leading to a higher reverse saturation current and a lower V_{oc} value.

Table 4.3 One-sun parameters of an all-Al cell and a control cell with an Ag front electrode

	Al electrode	Ag electrode
V_{oc} (V)	0.627	0.635
J_{sc} (mA/cm^2)	36.8	36.8
FF (%)	77.1	77.6
η (%)	17.8	18.1

4.4.3 Summary

An all-Al n-type rear junction monocrystalline Si solar cell with an efficiency approaching 18% is demonstrated by electroplating Al as the electrode on the front side of an n-type Si solar cell with a screen-printed Al rear junction. This cell shows excellent resistance to Al spiking, with only 0.5% absolute drop in its efficiency from its peak efficiency after annealing at 450˚C. Compared with a p-type all-Al front junction cell we reported before, whose efficiency is reduced to 75% of its initial value after annealing at 400˚C, the n-type rear junction cell keeps over 97% of its initial efficiency. The performance of the all-Al n-type cell is compared with a control cell which has a screen-printed Ag front electrode but otherwise identical to the all-Al cell.

4.5 Conclusion

In this chapter, we demonstrated the feasibility of Al electroplating for cost-effective production of all-Al Si solar cells. A traditional structure p-type cell and an improved rear-

junction structure n-type cell were fabricated to show the performance of electroplated Al front electrode. With the p-type cell, electroplated Al was first introduced to the Si solar cell fabrication with a decent efficiency of 14.6%. The detailed characterization showed the possible causes that affected the cell performance. Both series and shunt resistances have room to be improved. With the n-type cell, an excellent 17.9% efficiency was achieved which is comparable to the cells from industrial production lines. Since the structure was modified where electroplated Al was far from the junction, the cell showed a better spiking resistant property in annealing than traditional p-type cells. Though the efficiency of either of the cells is still lower than the public record Cu electrode cells, it is due to the limited fabrication environment not the process of Al electroplating. It provides an option when the PV industry decides to move away from Ag and produce Ag-free Si solar cells.

5. LIGHT-INDUCED ELECTROPLATING OF ALUMINUM ON SILICON

5.1 Introduction

With Al electroplating introduced to solar cell fabrication, a Si solar cell with ~18% efficiency has been demonstrated [47-49] in Chapter 4. However, because of the high-resistive solar-grade Si substrate, the potential across the cell is not constant in direct electroplating, thus it is impossible to achieve a uniform Al layer. In this case, a nickel (Ni) seed layer is employed to convey the current before Al electroplating [46]. With the Ni seed layer, the current distribution along the busbar and the finger are more uniform in the electroplating. Though Ni is widely used in the semiconductor process, it is an unnecessary process which fails to take the advantage of the compatibility between Si and Al. Thus, a novel method without Ni seed layer is in demand to further cut down the process cost.

Light-induced plating was developed for Si solar cell metallization in 1970s [59, 60] and has been used in cell fabrication for different metals including Ag, Ni, and Cu [61-64]. Fraunhofer ISE started to employ this method since 1992 to thickening the evaporated Ti-Pd-Ag contacts of high-efficiency solar cells [17]. A. Mette applied light-induced plated Ag on screen-printed solar cells to achieve high aspect ratio front electrode [63]. S.W. Glunz reported the concept of a two-step process: depositing a seed layer in the first step and reinforcing it with a highly conductive metal in the second step by light-induced plating[65]. The idea of light-induced plated Ni as the front electrode was introduced in [66]. Then many papers reported the method of light-induced plating of Cu on top Ni as the front electrode[67-70]. Nowadays, light-induced plating becomes one of the standard processes for the electroplated metal electrode Si solar cell.

Though the research on light-induced plating of Ni/Cu electrode is attracting the most attention, we are not ignoring the drawbacks of this method. Cu is an active metal which is detrimental to the minority carrier lifetime of Si, which is the reason why Ni seed layer is always required to serve as a barrier. However, the reliability of the fabricated solar cells is not promised with the possibility that Cu would penetrate the Ni layer and diffuse into Si body. Especially, additional annealing is required as Ni silicide formed at 350-450ºC gives the lowest contact resistivity. It makes Cu not the best choice as the electrode for Si solar cell.

Compared to Cu, Al has no issue with Si if the process temperature is kept low. Meanwhile, Ni seed layer is never required when light-induced plating is employed for the deposition of Al. It will significantly simplify the whole process. As the conventional electroplating of Al in the ionic liquid is developed in our lab, we are motivated to further develop the corresponding light-induced plating, and then apply it to solar cell fabrication. In this chapter, section 5.2 explains the basic idea and theory of light-induced plating technique. Section 5.3 reports the initial results of a simple method that light-induced plating of Al on Si is carried out in a small beaker. Section 5.4 reports a modified method that the backside Al is isolated from the ionic liquid. A new tool was designed to achieve it and the deposited Al is characterized. This work demonstrated the light-induced plating of Al directly on Si surface and confirmed the feasibility of applying this method to Si solar cell fabrication.

5.2 Theory of Light-Induced Plating

Light-induced plating takes the advantage of the photovoltaic effect of the solar cell to achieve electroplating. The photovoltaic current, generated in the p-n junction under illumination, is used to drive the process of electroplating. The electron-hole pairs (EHPs) excited by photons are separated by the built-in voltage. Since it is the electrons not holes are used for electroplating, the n-type Si of the p-n junction is required to expose to the electrolyte allowing electrons to flow out. The metal ions capture the diffused-out electrons and are reduced to metal deposited on the Si surface.

The schematic of the light-induced plating for solar cell metallization is shown in Fig. 5.1 [63]. The solar cell is placed in an electroplating bath with the backside connected to the cathode. The anode is the sacrificial metal supply to be plated as the front contact. When the solar cell is under illumination, the electroplating process starts with the photovoltaic current. A protective positive voltage is applied between the anode and the back contact to prevent the dissolution of the backside metal.

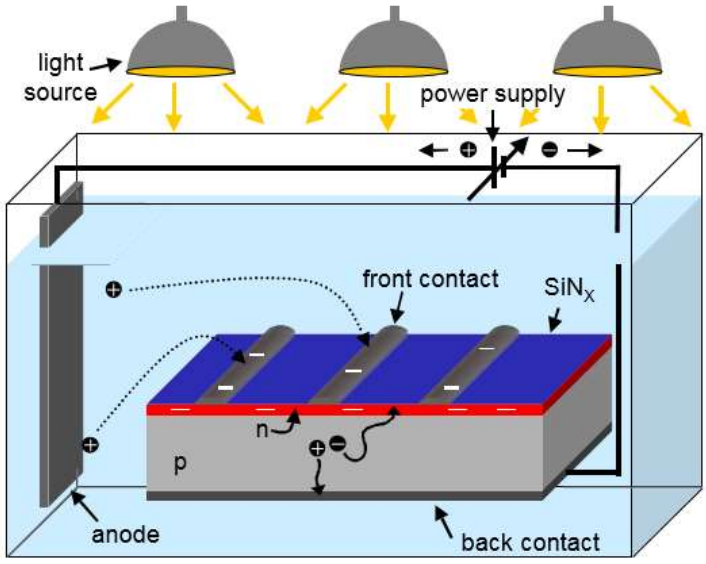

Fig. 5.1 Schematic of the light-induced plating process.

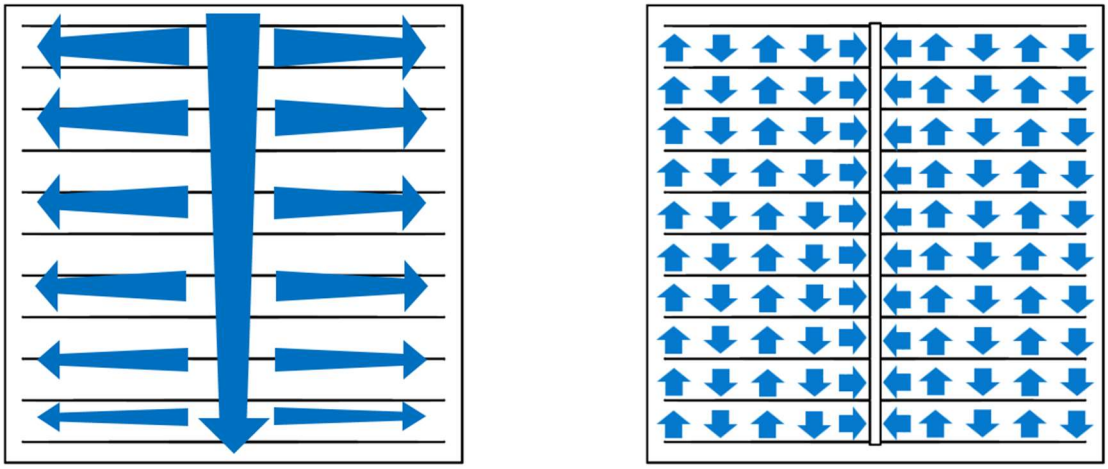

(a) (b)

Fig. 5.2 Schematic of the current flow in (a) traditional electroplating, (b) light-induced plating.

Compared to traditional electroplating, light-induced plating does not rely on the seed layer to convey the current. The self-generated current is evenly distributed all over the cell area, thus the deposited metal layer is uniform. As shown in Fig. 5.2, the current flow in traditional electroplating is along the busbar and then fingers. If the resistance along the current path is not low enough, there is a potential drop and the current density is small at the fingertips, thus thinner metal is deposited here. For light-induced plating, the current generated in the cell flows to the closest finger opening and delivers electrons to the electrolyte. Hence, the metal grow-rate is expected to be constant on all the fingers and thus the finger height is more uniform.

Based on the knowledge of traditional Al electroplating, we can design the light-induced plating of Al experiment, though there is no reported result of it as of now. When the substrate is illuminated, the EHPs were generated and separated by the p-n junction built-in field and the electrons diffused to the surface of n^+-Si. As shown in Fig. 5.3, the $Al_2Cl_7^-$ ions captured the electrons and formed Al on the Si surface, according to the reaction [55]:

$$4Al_2Cl_7^- + 3e^- \leftrightarrow Al + 7AlCl_4^-$$

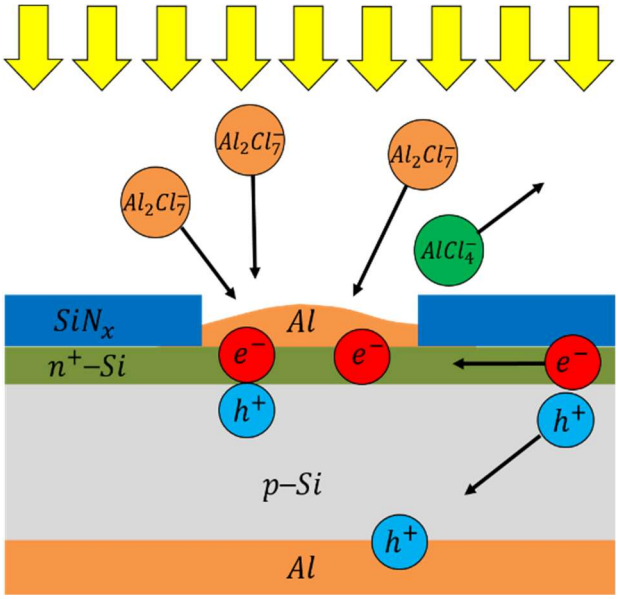

Fig. 5.3 Principle of light-induced Al plating on n side of a Si p-n junction.

5.3 Simple Light-Induced Plating of Al in Ionic Liquid

Though light-induced plating is achieved in aqueous solutions for Ni, Cu, and Ag, it is not seen in non-aqueous ionic liquid for Al. In this section, the light-induced plating of Al on Si surface is achieved in a small beaker. The suitable wavelength range is extracted to determine the light source by spectroscopy and quantum efficiency test for experimental set-up. Adhesive and solid Al is replicable obtained at different temperatures. The structure and composition are characterized by SEM and EDX while the resistivity is tested with a probe station.

5.3.1 Experimental

The preparation process of ionic liquid described in Chapter 4 is not repeated here. Light-induced plating requires a light source with a suitable wavelength. It is determined

by the transmission spectrum of the electrolyte and the absorption spectrum of Si. The transmission spectrum of the electrolyte was measured in a quartz cuvette by spectrophotometry, as shown in Fig. 5.4. The absorption spectrum of Si was characterized with an external quantum efficiency tester, as shown Fig. 5.5. The product of the two spectra at different wavelengths provides the suitable wavelength range for light-induced Al plating on Si in the ionic liquid, as shown in Fig. 5.6.

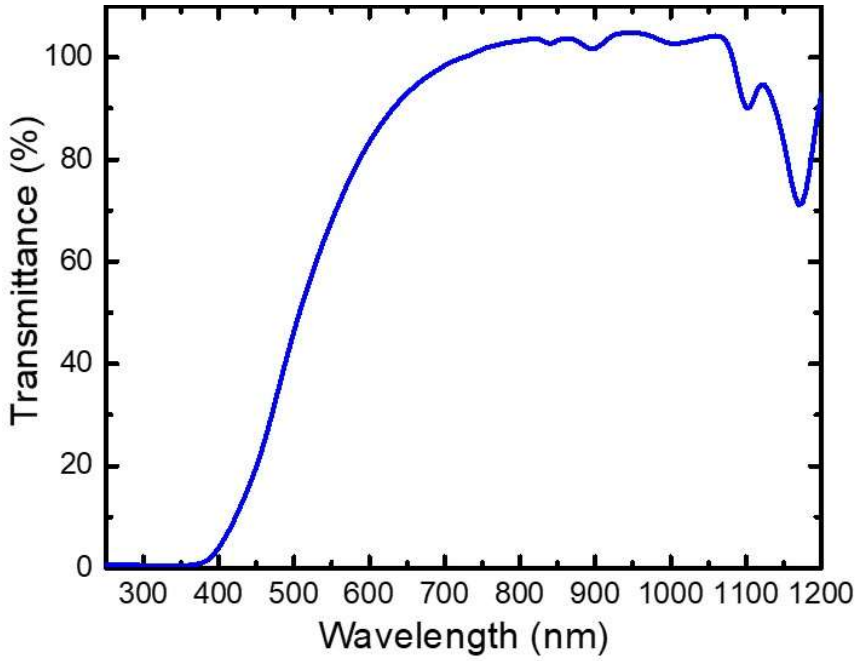

Fig. 5.4 Transmittance of ionic liquid as a function of wavelength.

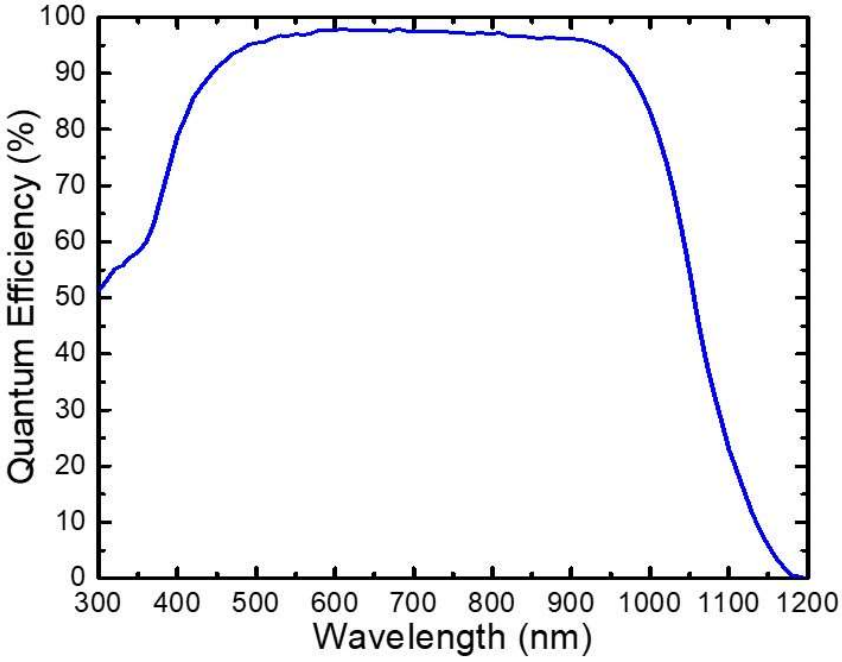

Fig. 5.5 External quantum efficiency of Si solar cell substrate.

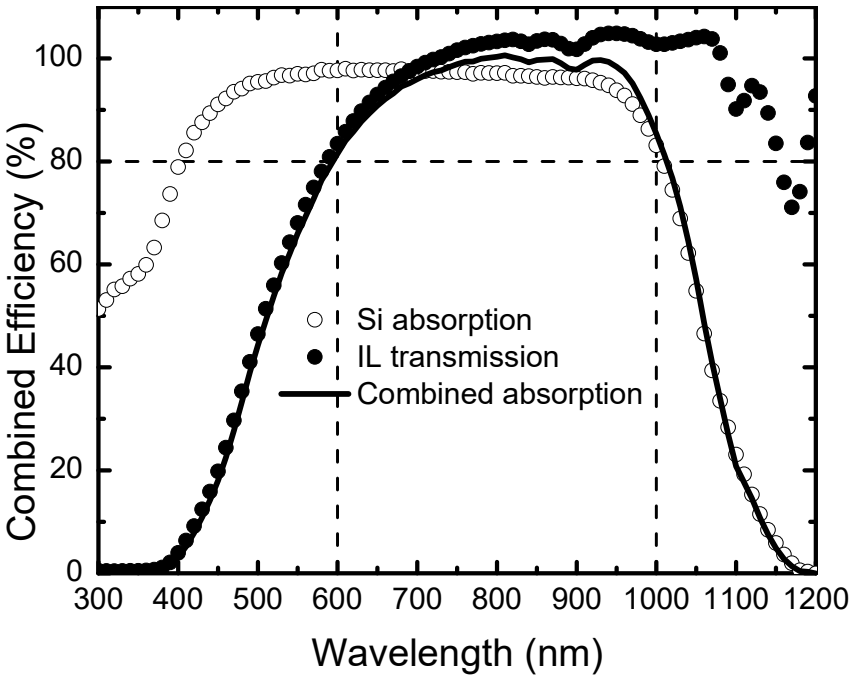

Fig. 5.6 Suitable wavelength range for light-induced Al plating on Si.

The wavelength should be between 600 nm and 1,000 nm for 80% absorption efficiency by Si. In this study, we chose red LEDs with a wavelength of 620 nm. The parameter of the red (LED) is listed in Table 5.1. The LED array is designed to cover the

whole sample area to be plated on, as shown in Fig. 5.7. it is adequate for research as the power of the LED array can supply enough current density.

Table 5.1 Parameters of Red LED

Diameter (mm)	5
Forward voltage (V)	2-2.2
Current (mA)	20
Power (W)	0.04
Wavelength (nm)	~620

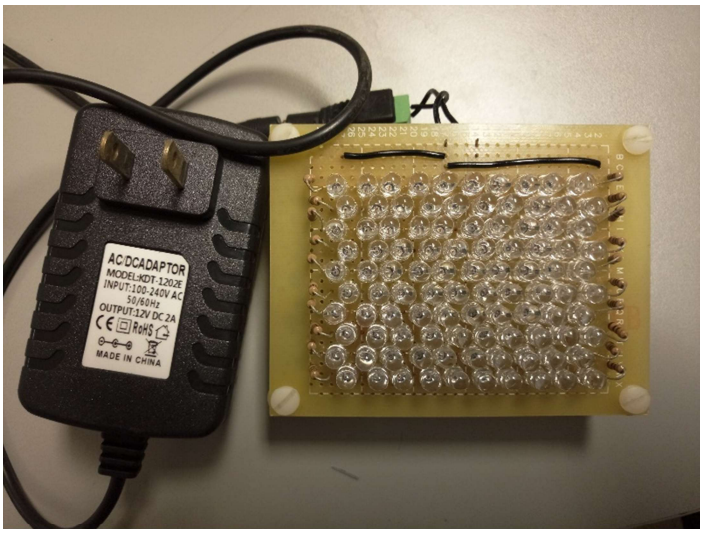

Fig. 5.7 Red LED array panel.

It is noted that the red LED array is not the best choice. For one thing, the highest efficiency near 100% lies at the infrared region of the spectrum between 800 nm and 950 nm. For the other thing, the degradation of the ionic liquid over time lowers the light transmission efficiency further. We observed it by measuring transmittance before and after the ionic liquid went through many experiments, as shown in Fig. 5.8. The red region dropped below 40% while the infrared region stayed over 80%. Hence, infrared LED should be considered for experiment and production in the future.

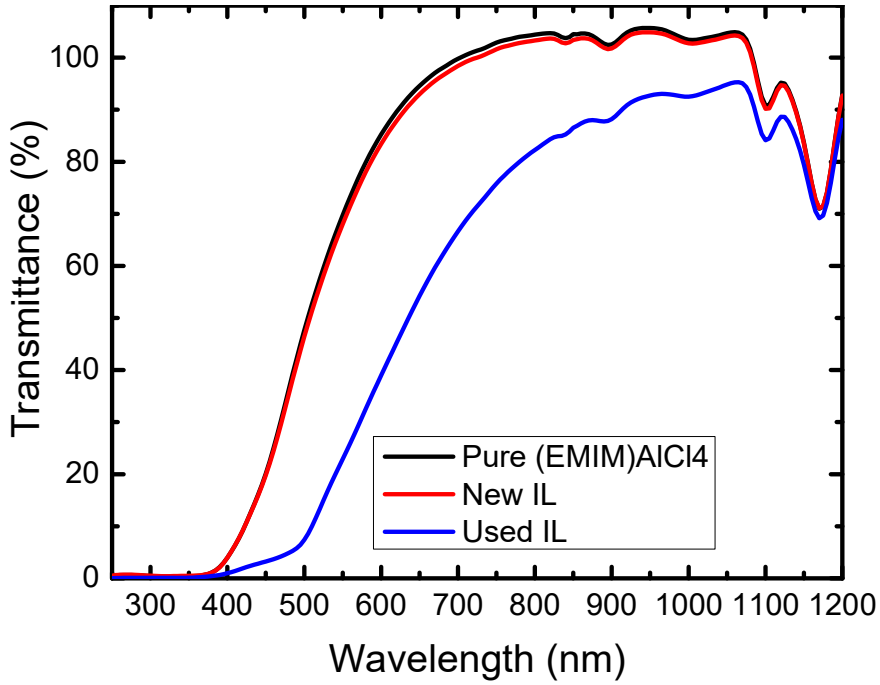

Fig. 5.8. Transmittance of ionic liquid before and after cycles of experiments

The sample was prepared from a half-processed solar cell (Canadian Solar) with silicon nitride (SiN_x) covered n^+-Si front side and screen-printed Al on the back side. The front side was patterned with laser ablation where SiN_x was removed and Si was exposed. Two types of openings were designed: (1) square window 0.5×0.5 cm^2 (2) lines 1×0.05 cm^2. The openings were cleaned in 2% HF for 30s to remove the native oxide on it. To reduce the laser damage and improve adhesion, a 3% NaOH cleaning for 1.5min at room temperature was applied to etch off a thin surface layer. It was followed by HF cleaning again and blowing dry. The backside and edges were covered with Teflon tape to prevent it touching the ionic liquid and interrupting the current path.

The schematic and actual set-up of the experiment are shown in Fig. 5.9. The current density was adjusted to 40mA/cm^2 for an hour by the Galvanostat. After the experiment, the sample was rinsed with methanol and flowing water and then blown dry with nitrogen.

The experiments were performed at different temperatures at 75ºC. The morphology and composition of the deposited material were characterized by scanning electron microscope (SEM) and energy dispersive X-ray analysis (EDX). A profilometer and a probe station were used to measure the thickness and the resistance individually.

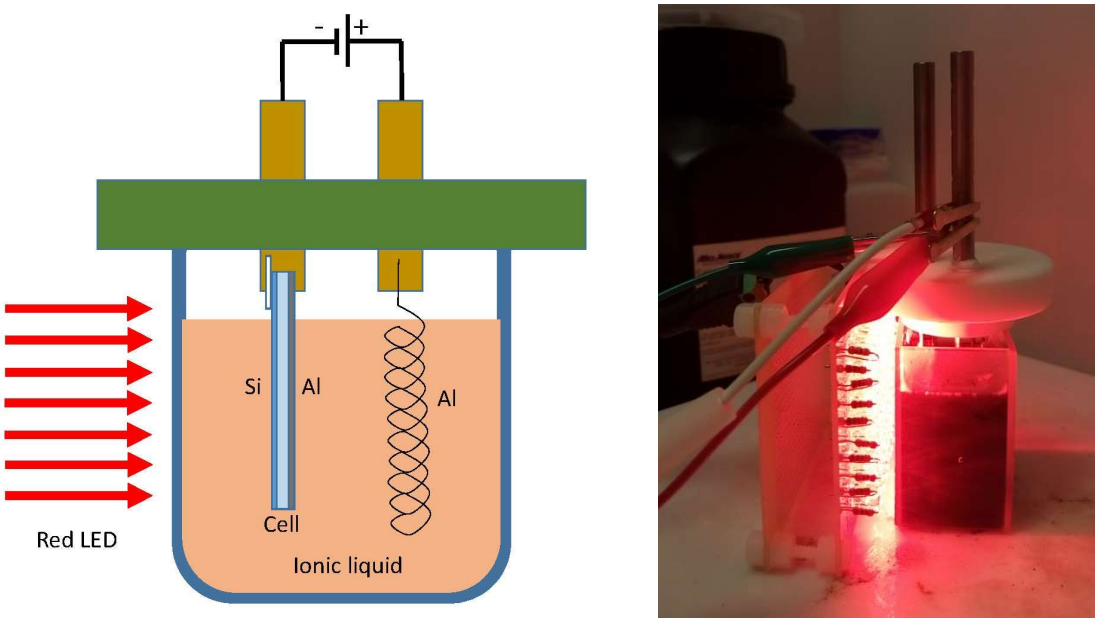

(a) (b)

Fig. 5.9 Experimental set-up of light-induced plating (a) schematic, (b) actual.

5.3.2 Results and Discussion

The light-induced plating was first carried out on square-window samples. The experiments initially failed before the NaOH cleaning was introduced. The plated Al stayed on the sample when taken out of the ionic liquid. However, the adhesion was very poor as it dropped off the sample during DI water rinsing or N_2 blowing. This is possibly because of the laser damage or contamination during shipment. As NaOH can etch Si slowly at room temperature, it is employed for cleaning the surface. With NaOH etching, the Al is adhesive to the Si surface after the experiment, as shown in Fig. 5.10.

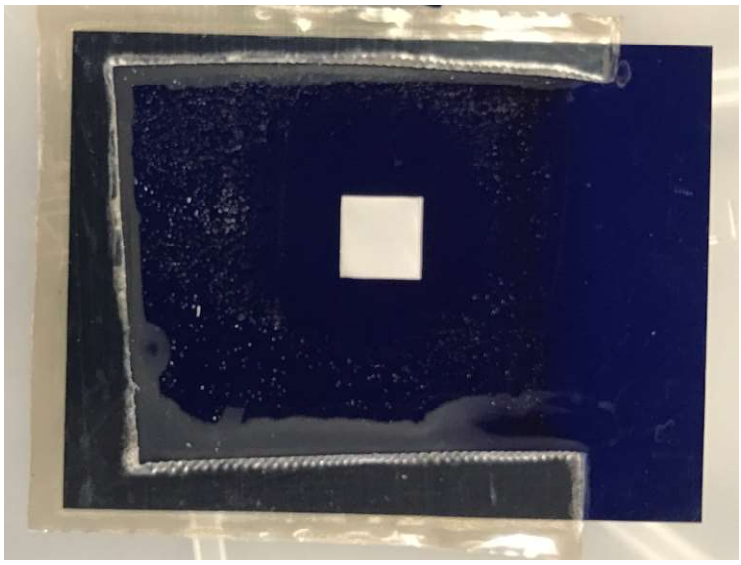

Fig. 5.10 Plated Al on window pattern Si solar cell substrate

Fig. 5.11 shows the SEM image and EDX analysis of the plated Al. The Al is continuously covering the Si surface. The surface morphology is similar to what we have achieved in traditional electroplating, which verified the success of the Al light-induced plating. The EDX analysis shows a strong peak of Al and minor impurities of O and Cl. The reason for the unusually existing high C peak is not clear. It may be attributed to contamination from the Teflon tape during operation.

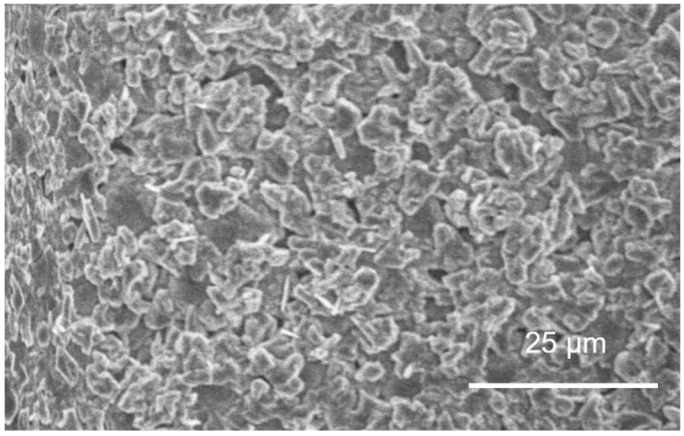

(a)

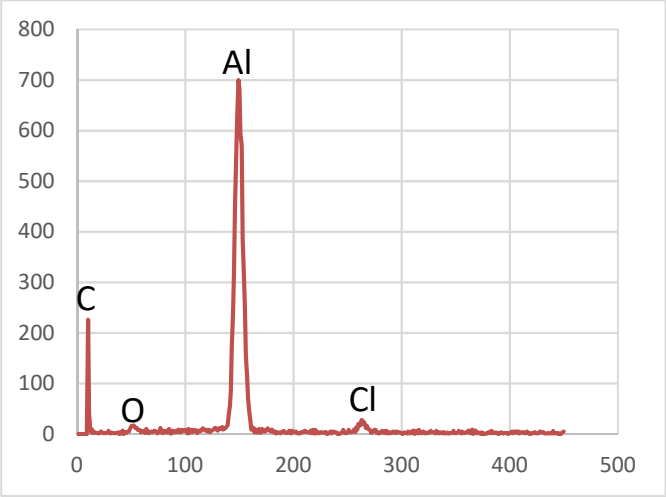

(b)

Fig. 5.11 (a) SEM image of light-induced plated Al, (b) Corresponding EDX analysis.

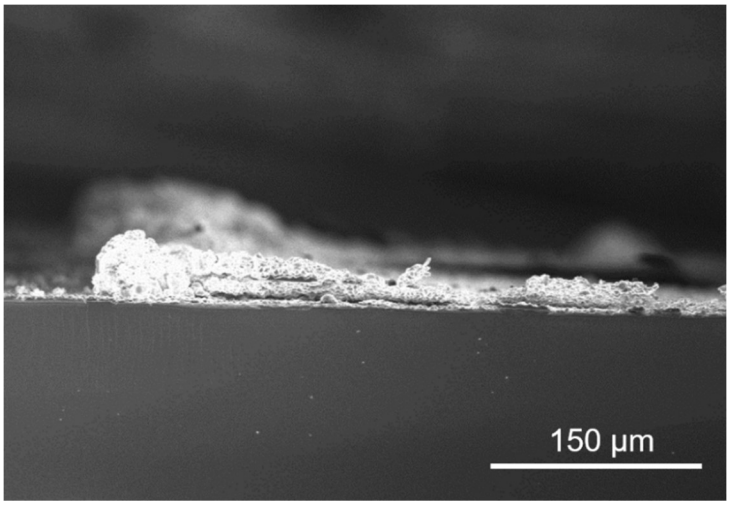

Fig. 5.12 Cross section of the plated Al.

The cross-section of the plated Al is shown in Fig. 5.12. We see the Al at the window edge is thicker than the center, meaning the uniformity is not achieved in this experiment. Compared to actual solar cell fingers, the plating window is kind of large that current is inclined to flow into the electrolyte from the edge. Thus, Al grows thicker at the edge than the center. This should not be an issue for solar cell fabrication, however, it prevents us to

accurately measure the resistivity of the plated Al with a simply 4-point probe test. Hence, we designed the lines pattern for resistivity measurement shown in Fig. 5.13.

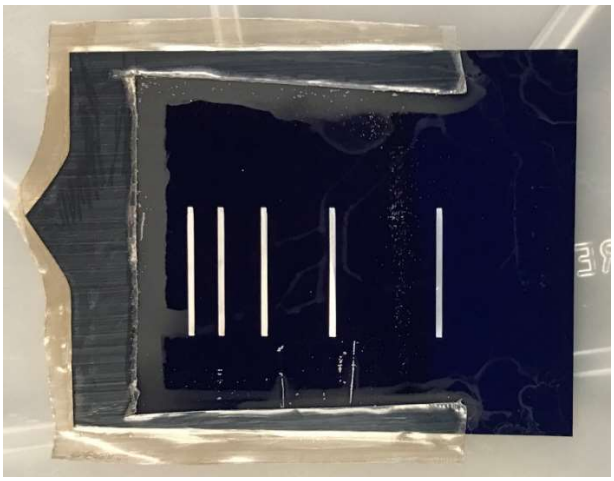

Fig. 5.13 Plated Al lines on Si solar cell substrate.

Table 5.2 Calculated resistivity of plated Al

Left (mm)	Middle (mm)	Right (mm)	Resistance (Ω)	Resistivity (Ω-cm)
7.7	5.8	6.8	0.1024	$(3.71\sim4.92)\times10^{-6}$
7.2	5.4	6.1	0.1234	$(4.16\sim5.55)\times10^{-6}$
7.5	7.1	9.8	0.1341	$(5.95\sim8.21)\times10^{-6}$

The resistance of the Al lines was measured by a 4-probe station to eliminate the effect of contact resistance. The thickness of Al lines was measured by a profilometer on average of left-middle-right positions. It is noted this is not an accurate method to measure the thickness, but it can be used to estimate the possible resistivity range. With the designed 10×0.5 mm^2 area, the resistivity is extracted by the measured resistance and thickness. Table 5.2 shows the calculated resistivity on 3 lines while 1 line is excluded as an outlier. The resistivity is in the range of 10^{-6} Ω-cm, which is comparable to the traditional Al

electroplating as well as screen-printed Ag. The result proved that it is possible to apply light-induced plating of Al as the front electrode of Si solar cell.

There is still one big issue with the current process. It is hard to handle the operation covering the backside and edge with a Teflon tape, and the sample is easy to break when peeling off the tape. Meanwhile, the tape may also introduce contamination into the sensitive ionic liquid. This is not acceptable for real solar cell production, so a new and convenient experimental set-up is required for future development.

5.3.3 Summary

In this section, the light-induced plating of Al on a half-processed Si solar cell substrate is first demonstrated. The Al is continuous and dense with good adhesion to the Si surface. A lower range of 10^{-6} Ω-cm resistivity is proved to be achievable, comparable to screen-printed Ag as well as the traditional electroplated Al. To facilitate this process for solar cell fabrication, a new set-up that simplifies the process is required for further research.

5.4 Light-Induced Plating of Al in a Modified Tool

The light-induced plating of Al is carried out in the last section. However, the operation process is complicated with the Teflon tape cover, so it is hard to achieve repeatability and reliability in further solar cell fabrication. Since we are focusing on the promotion of this technique to the photovoltaic industry, the ease of use is important for this process.

5.4.1 Experimental

The schematic of the new set-up is shown in Fig. 5.14. A Teflon holder with a rectangle center hole was designed to carry the sample. The sample was put in the holder with the

lines on the front side facing down through the hole and fixed by the pressure from the tightened Al screws. The Teflon holder was then put into the container with the ionic liquid. The sample surface was 5mm to the bottom so the lines were fully contacted with the solution. As no gap was left between the sample and the Teflon holder, the back side was kept dry and no liquid was expected to get on it. A pure Al mesh was put below the holder and used as the sacrificing anode to provide Al ions. The cathode was connected to the back side Al. A red light-emitting diode (LED) array with 620 nm wavelength was put below the tank and covered the whole sample area. The electrolyte was filled into the crystallizing dish and the solution depth is ~10mm. The container was wrapped with a temperature adjustable heating tape and put on a stage with a 60mm diameter round hole in the center.

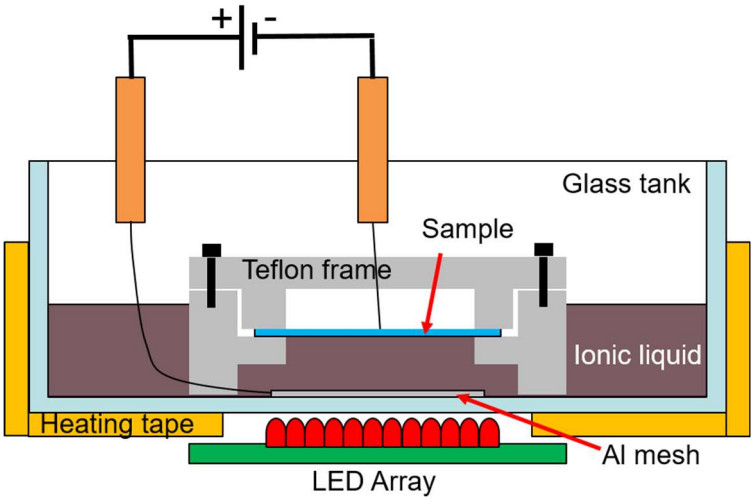

(a)

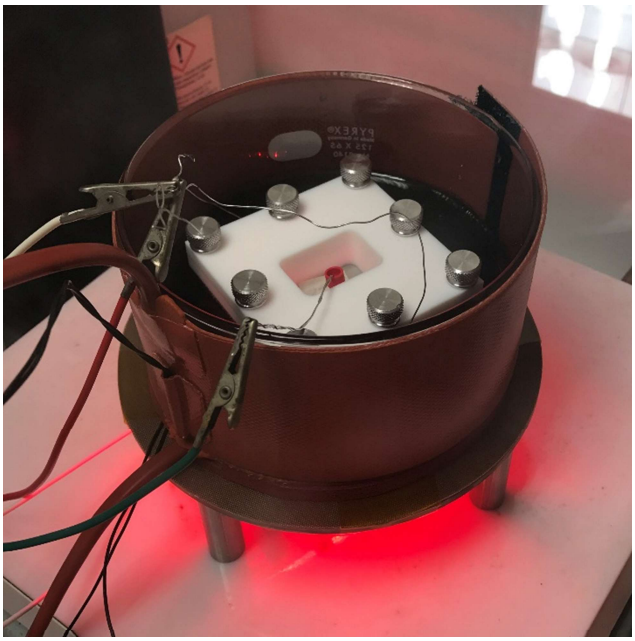

(b)

Fig. 5.14 Experimental setup for light-induced Al plating on Si (a) schematic, (b) actual.

The sample was a partially-processed Si solar cell from Canadian Solar. It had a 75-nm silicon nitride (SiN_x) layer covering the n^+ side and screen-printed Al on the p side. The SiN_x layer was patterned with openings of 10×0.5 mm^2 by laser ablation where Si was exposed. The sample was cleaned in 2% hydrofluoric acid (HF) for 30 s and then immersed in 3% sodium hydroxide (NaOH) for 15 s at room temperature to remove laser damage. With a final HF dip, the sample was placed on the sample holder with the pattern facing down. The pattern was in contact with the electrolyte. The backside Al on the sample served as the cathode for plating. The voltage applied between anode and cathode was controlled by a Gamry Reference 3000 potentiostat to achieve a plating current of ~40 mA/cm^2. The plating was performed at different temperatures from 25ºC to 70ºC.

5.4.2 Results and discussion

The textured front surface of Si solar cells is not a perfect substrate for electroplating. There are random-distributed 1 μm size pyramids all over the surface and the laser ablation further

creates damages. Though we achieved Al electroplating directly after the HF clean, the process was not stable and sometimes the deposited Al fell off the surface during rinsing or blowing. NaOH is widely used in solar cell fabrication for texturing and can etch off Si. Since the etching rate is controllable [71], we applied the NaOH etching before the plating process and the adhesion is improved. Fig. 5.15(a) and (b) show the SEM images of the top-view of the Al deposited at 25ºC and 60ºC. In both cases, the Al is continuously covering the Si surface. The Al crystallites are denser and smaller for 25ºC in Fig. 5.15(a) while they are larger and flake-like for 60ºC in Fig. 5.15(b). The morphology shows that lower temperature helps to achieve compact and uniform Al layer on the surface in light-induced plating at 40mA/cm^2. Fig. 5.15(c) shows cross-section SEM image of the 25ºC sample and the corresponding EDX analysis. It is also shown the deposited Al layer is dense and uniform on the Si surface as in Fig. 5.15(a). The strong peak at 1.49keV in EDX analysis verified the composition of Al, as shown in Fig. 5.15(d). The minor peaks of O and Cl are residuals from the ionic liquid. It is still under investigation of the optimal experimental condition for light-induced plating of Al on Si, especially previous reports showed the high temperature at 90ºC improved the uniformity for traditional electroplating of Al on copper [72].

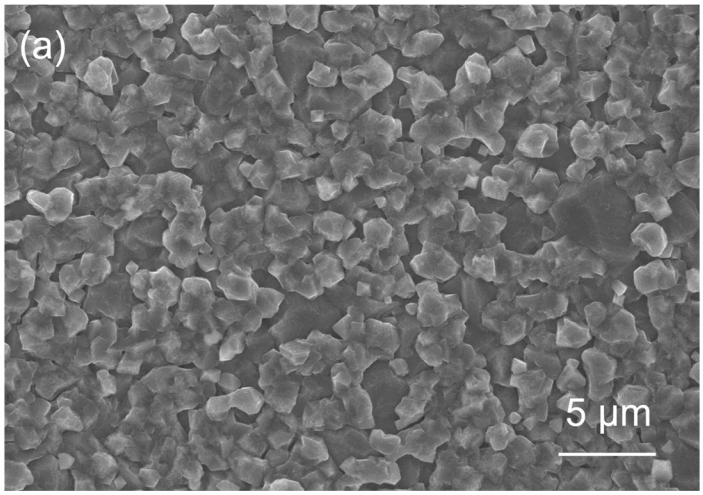
(a)
5 μm

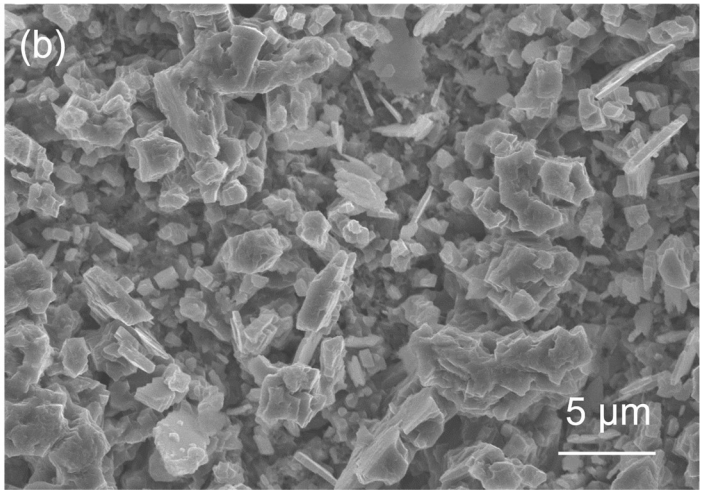
(b)
5 μm

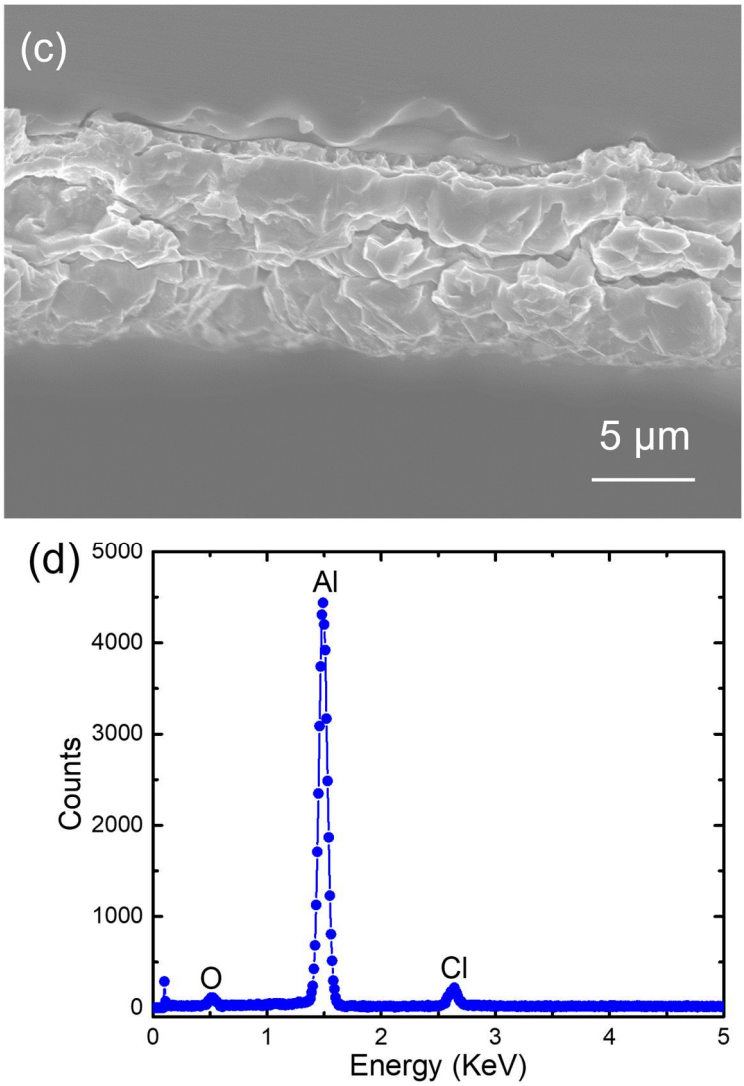

Fig. 5.15 SEM images of plated Al at the temperature (a) 25ºC, (b) 60ºC, (c) Cross section of (a), and (d) EDX analysis of (a).

The thickness of the Al films was measured by a profilometer. Fig. 5.16(a) shows the average thickness at different plating temperatures. Although the plating current and time were kept consistent, the average thickness and its variation increased with temperature. The resistance of the Al films was measured with a four-probe method. With the Al film dimensions of 10×0.5 mm^2, the resistivity of the Al films was extracted. Fig. 5.16(b) shows the resistivity of the Al films as a function of plating temperature. The lowest average resistivity is ~4×10^{-6} Ω-cm at 25ºC, which is about 1.5 times that of bulk Al. It is lower

than the resistivity of ~7×10^{-6} Ω-cm by conventional Al electroplating we reported before [47]. However, the resistivity becomes larger and its fluctuation also larger as the temperature increases. This agrees with the SEM images in Fig. 5.15. Since the Si surface is textured, light-induced Al likely grows at the tips of the pyramids and it is possible that high temperatures aggravate the nonuniformity of the Al deposits. The thicker Al deposits at higher temperatures suggest higher plating rates, but the higher resistivities indicate less dense or more porous Al deposits. Meanwhile, lower temperatures might reduce the diffusion of Al ions away from the concave positions on the surface. Another possibility is that moisture is recaptured by the ionic liquid at temperatures below 100ºC. As the ionic liquid is in an open tank, it has a large surface area to absorb moisture. It is recommended that the plating process is carried out in an inert ambient or heated to above 100ºC. Further investigation is underway to optimize the film uniformity and density.

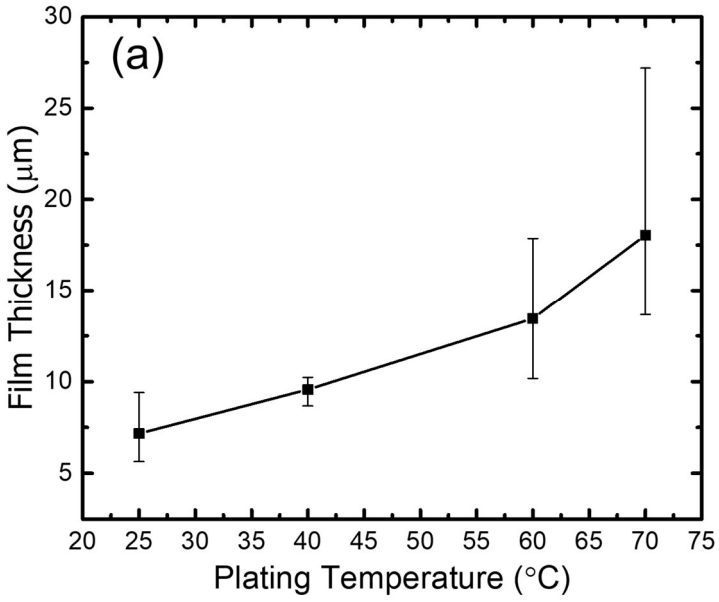

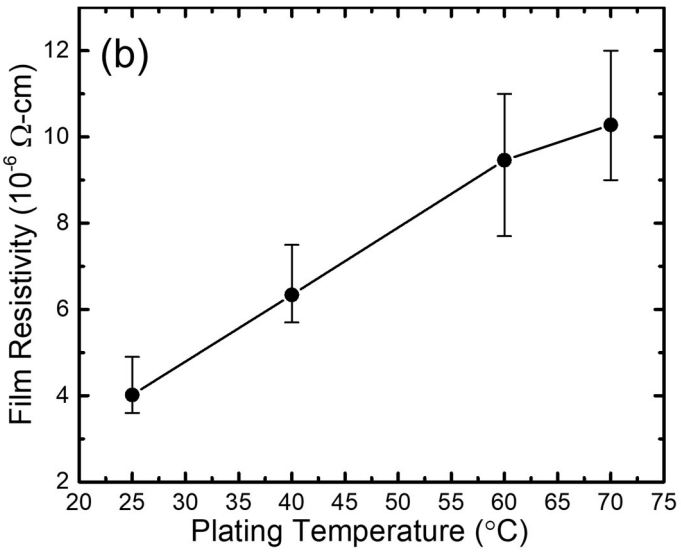

Fig. 5.16 (a) Thickness and (b) resistivity of light-induced Al films as a function of plating temperature.

Although the plating current is mainly determined by the light intensity in light-induced plating, the ion concentration in the electrolyte also plays a significant role in plating current. Cyclic voltammetry was used to monitor the Al concentration in the electrolyte. Ionic liquids were prepared with different molar ratios of $AlCl_3$ to (EMIm)$AlCl_4$ from 0.125 to 0.75. Two Al wires (≥99.99%, Aldrich) were used as the working and counter electrodes. The reference electrode was connected to the counter electrode. With the applied voltage sweeping from 0 V to –2 V, the current was recorded as shown in Fig. 5.17(a). When the molar ratio is less than 0.375, there is no clear current peak. This suggests that the electrolyte is not a Lewis acid yet and Al plating does not occur for molar ratios below 0.375. When the ratio is above 0.375, the peak current increases with Al concentration. A linear fit is extracted for the relationship between peak current and Al concentration as shown in Fig. 5.17(b). This can be used to monitor the Al concentration in the electrolyte as it may be depleted during plating.

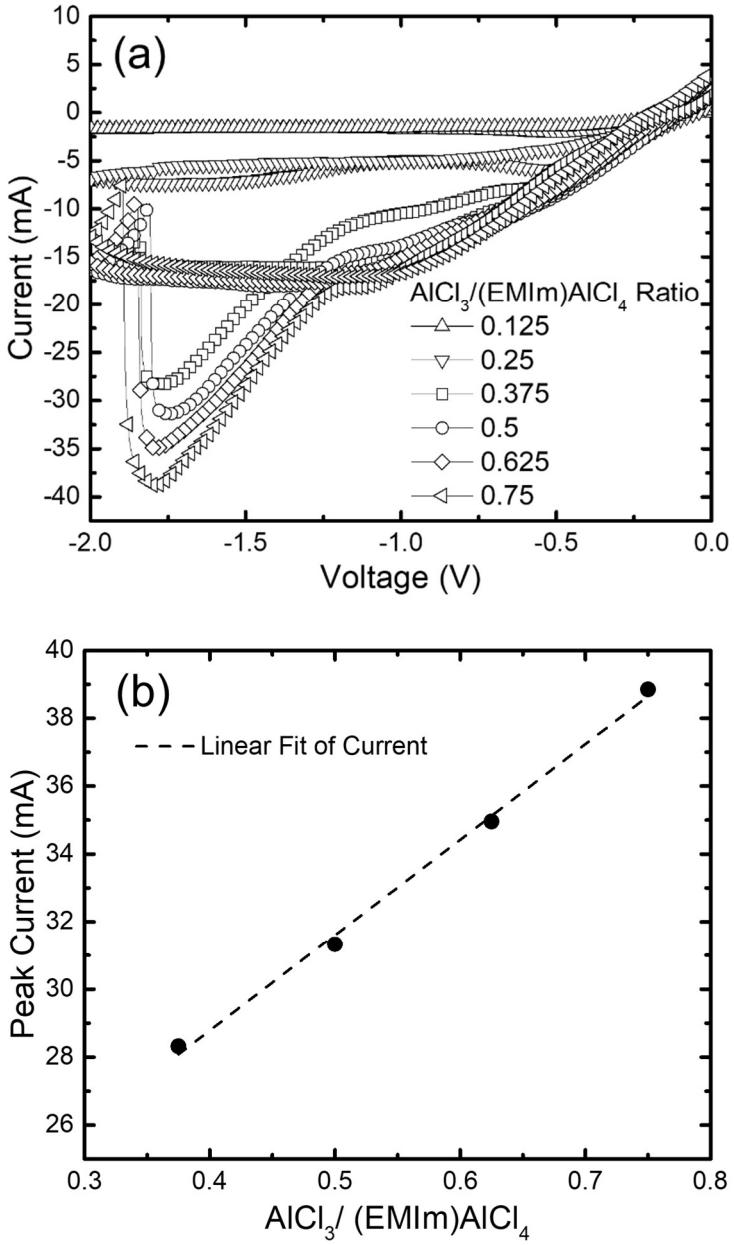

Fig. 5.17 (a) Cyclic voltammetry at different $AlCl_3$/(EMIm)$AlCl_4$ ratios and (b) relationship between peak current and $AlCl_3$/(EMIm)$AlCl_4$ ratio.

5.4.3 Summary

A new experimental set-up is employed for light-induced plating of Al, which simplified the operation and enhance the repeatability. With the new tool, Al is uniformly deposited on the Si surface with a low resistivity. A simplified CV method is proposed to

monitor the ion concentration in the ionic liquid. It provides a solution for applying the technique to production of Si solar cell.

5.5 Conclusion

Light-induced plating of Al on a Si substrate with a p-n junction is implemented in an ionic liquid. Adhesive and low-resistivity Al can be directly deposited on Si without a seed layer as in conventional electroplating. The lowest resistivity demonstrated is $\sim 4\times10^{-6}$ Ω-cm. Higher plating temperatures seem to increase the plating rate but have a negative effect in the current plating setup as it increases the resistivity and its fluctuation of the Al deposits. The suitable wavelength range for the light source is found to be between 600 nm and 1,000 nm. Cyclic voltammetry is proposed to monitor the Al concentration in the ionic liquid. This work paved a promising and economical way to replace Ag with Al in Si solar cell manufacturing.

6. EFFICIENCY ANALYSIS AND CONTROL BY NUMERICAL SIMULATION

6.1 Numerical Simulation

Numerical simulation or TCAD software is an efficient tool widely used in semiconductor industry to design new devices, characterize parameters, and optimizing behaviors. Since the solar cell is a large area PN junction in structure and contains a variety of physical effects, it is suitable to resort to TCAD tools for optimization. However, the PV industry relies more on engineers' experience and basic calculation rather than a thorough quantitative analysis, given the solar cell structures resembled each other in the past years [73]. PC1D is the most commonly used solar cell modeling program due to its fast speed and user-friendly interface, but it failed to show more distribution details and contains insufficient physical models. Since making progress in energy conversion efficiency is driving companies to be more competitive in PV market, numerical simulation tool will be a promising method in solar cell design and modification.

The numerical software Synopsys Sentaurus as well as Silvaco Atlas are famous and become widely used in photovoltaic research. Most of work is focused on modeling new concept solar cells with complicated structures, not close to the mainstream production. In this work, solar cells parameters' sensitivity to process is studied, which provides manufacturing companies a possible solution to efficiency dispersion.

The simulated cell structure is shown in Fig. 6.1, which is the most common of commercial cells today. With the symmetry of the cell, a half cell is simulated to reduce the computation time. P-type monocrystalline-Si is used as the substrate. The front contact is Ag and the antireflection coating is SiN_x. The n^+ emitter is formed by phosphorus

diffusion in Sentaurus to mimic $POCl_3$ diffusion. The back contact is Al and an additional p^+ layer is introduced between Al and Si to represent the back-surface field (BSF).

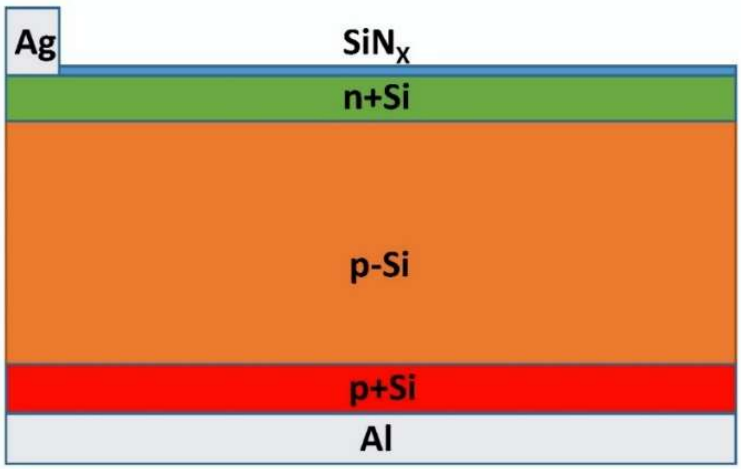

Fig. 6.1 Schematic of the cell structure simulated in this study.

The parameters for the cell structure simulated are listed in Table 6.1. The thickness of the n+ emitter is not fixed because it varies with diffusion conditions. The reference substrate doping is 1×10^{16} cm^{-3} and the p^+ BSF has a doping concentration of 1×10^{19} cm^{-3}. The surface recombination velocity at the SiN_X/Si interface is fixed to 1000 cm/s. Physical models employed in the simulation [74] include Fermi-Dirac carrier statistics, band gap narrowing, incomplete ionization and bulk recombination including SRH, Auger and radiative. A doping-dependent contact resistivity model is used for the front and back contacts. The illumination source is the AM 1.5G spectrum and the optical solver is transfer matrix method (TMM).

Table 6.1 Parameters of the simulated cell structure

Parameter	Description	Value (μm)
W_{fc}	Half width of front contact	35
W_{tot}	Half width of total cell	1500
t_{SiNx}	Thickness of ARC	0.075

t_{Si}	Thickness of Si wafer	200
t_{p+}	Thickness of BSF	10

6.2 Factors to Efficiency Loss

6.2.1 Diffusion Temperature

The diffusion temperature for p-type cells is typically ~850˚C. Since room-temperature $POCl_3$ and carrier gas N_2 flow into the diffusion furnace, the front end of the furnace is cooled and its temperature is lower than required. The temperature range in our simulation is 770–900˚C. The diffusion time is set to 20 min. It is followed by the removal of a 70-nm surface layer to represent the removal of the dead layer. The emitter doping profile from simulation is presented in Fig. 6.2, which is in agreement with the literature [73, 75]. Fig. 8 shows that the surface doping concentration varies between 9.2×10^{18} and 6.1×10^{20} cm^{-3}. The corresponding emitter sheet resistance is between 19 Ω/□ and 1425 Ω/□.

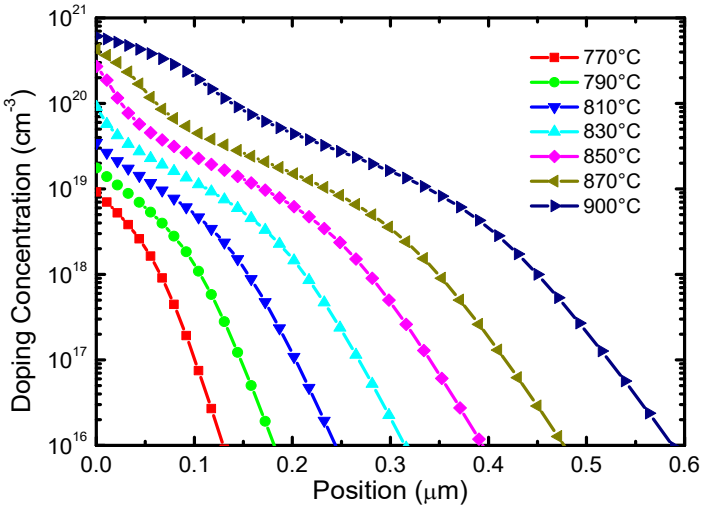

Fig. 6.2 Emitter doping profiles at different diffusion temperatures.

The effect of diffusion temperature on cell efficiency is shown in Fig. 6.3. For this simulation, efficiency peaks at ~830˚C. When the diffusion temperature drops to 770˚C, i.e. a 60˚C temperature reduction, the efficiency is lowered by 5.9% absolute. On the other hand, when the temperature increases by 70˚C to 900˚C, the efficiency is lowered by 2.4% absolute. The efficiency is significantly reduced at lower diffusion temperatures, which occur in batch diffusion furnaces. Diffusion temperature has multiple effects on cell efficiency. It affects the contact resistance of the front contact and controls the emitter resistance. It also impacts emitter recombination. Further simulations reveal the individual effect of each of these factors.

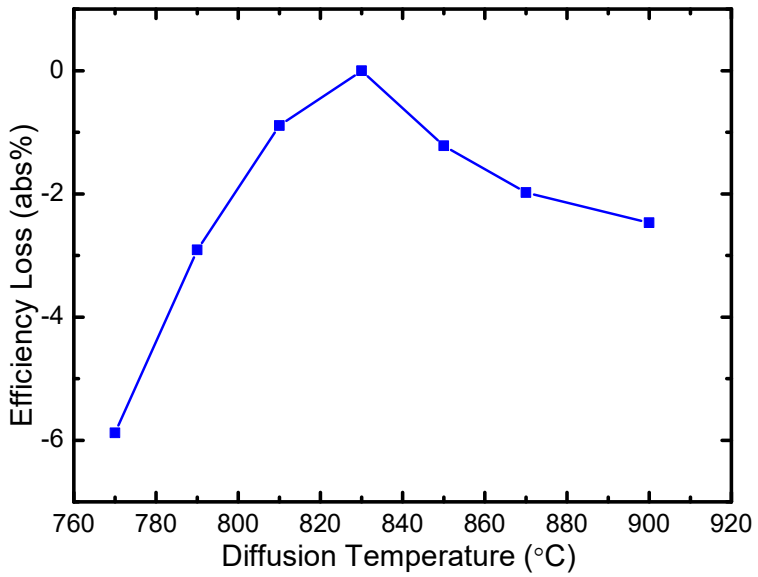

Fig. 6.3 Efficiency loss as a function of diffusion temperature.

For a given metal with a given Schottky barrier height, the contact resistivity relies on surface doping concentration. When the surface doping concentration changes from 1×10^{19} cm^{-3} to 1×10^{21} cm^{-3}, the contact resistivity varies from ~1×10^{-3} Ω-cm^2 to ~1×10^{-8} Ω-cm^2 [76]. In this simulation, the cell with 830˚C diffusion on a 1×10^{16} cm^{-3} wafer is chosen as the reference. This fixes the emitter sheet resistance and emitter recombination in the cell.

The contact resistivity is varied between 1 Ω-cm^2 and 1×10^{-7} Ω-cm^2, and its effect on cell efficiency is illustrated in Fig. 6.4. It is clear that the efficiency remains constant until the contact resistivity rises to 1×10^{-3} Ω-cm^2, corresponding to a surface concentration of 1×10^{19} cm^3. The typical surface doping concentration in production is higher than this value. Even if the contact resistivity increases to 1×10^{-2} Ω-cm^2, the efficiency loss is still less than 1% absolute.

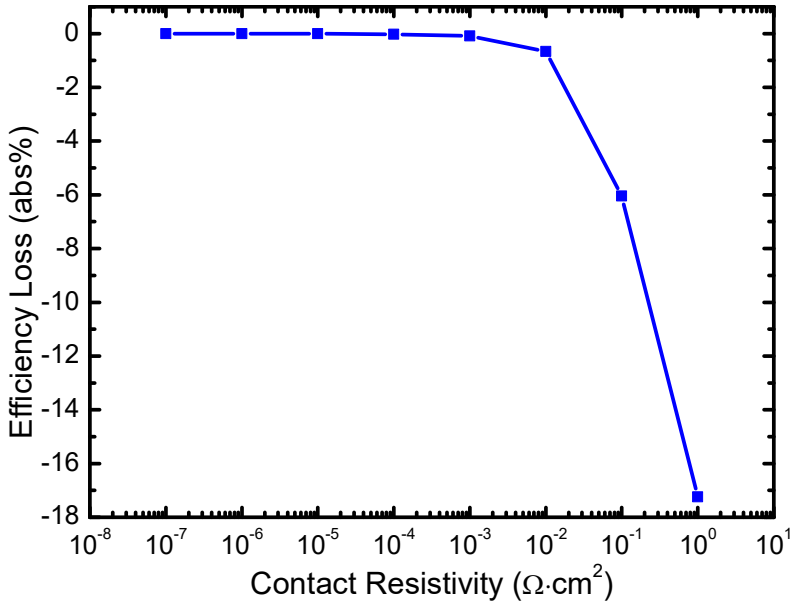

Fig. 6.4 Efficiency loss as a function of contact resistivity.

The emitter resistance, as represented by its sheet resistance, is controlled by diffusion. To extract the effect of emitter sheet resistance, a series of Gaussian doping profiles with sheet resistances ranging from 40 Ω/□ to 1750 Ω/□ are added as the n+ layer to the cell structure in Fig. 6.1. The contact resistivity is fixed to 1×10^{-5} Ω-cm^2 and the recombination model is turned off to focus on emitter resistance. The result is shown in Fig. 6.5. Using the efficiency from the smallest sheet resistance as the reference, the efficiency loss is ~1.2% absolute when the sheet resistance increases to 200 Ω/□ and reaches almost 8.5% at 1750

Ω/□. This suggests that the efficiency loss at lower diffusion temperatures as shown in Fig. 9 comes mainly from the resistive losses in the emitter, as lower temperatures lead to higher emitter sheet resistances.

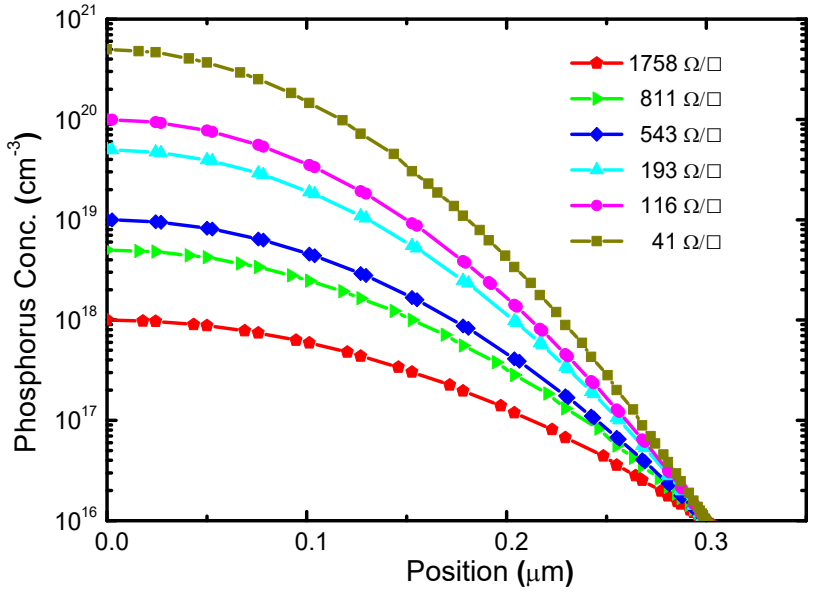

(a)

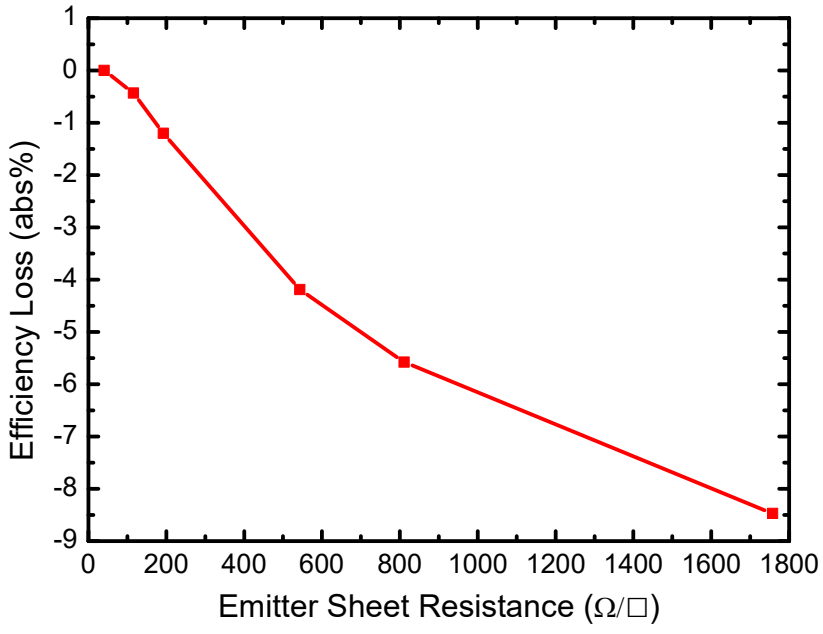

(b)

Fig. 6.5 (a) Emitter doping profiles at different surface concentration with same junction depth (b) Efficiency loss as a function of emitter sheet resistance.

High doping in the emitter results in high emitter recombination. To isolate the effect of emitter doping on emitter recombination, Gaussian doping profiles with surface doping concentrations ranging from 5×10^{19} cm^{-3} to 5×10^{20} cm^{-3} but fixed emitter sheet resistances (50, 100 and 150Ω/□) and a fixed contact resistivity (1×10^{-5}Ω-cm^2) are employed. The result is shown in Fig. 6.6. As expected, higher emitter doping concentrations lead to lower efficiencies for each emitter sheet resistance. The efficiency loss is 1.7–2% for the three sheet resistances considered. Meanwhile, the 100 Ω/□ cell has the highest efficiency among the three, i.e. the optimum emitter sheet resistance is ~100 Ω/□.

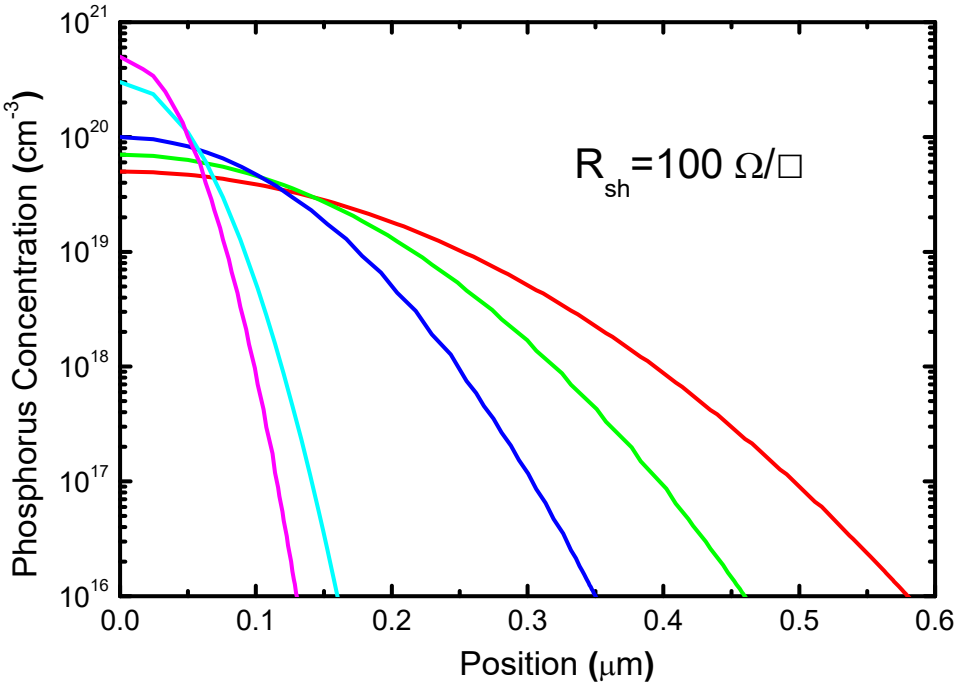

(a)

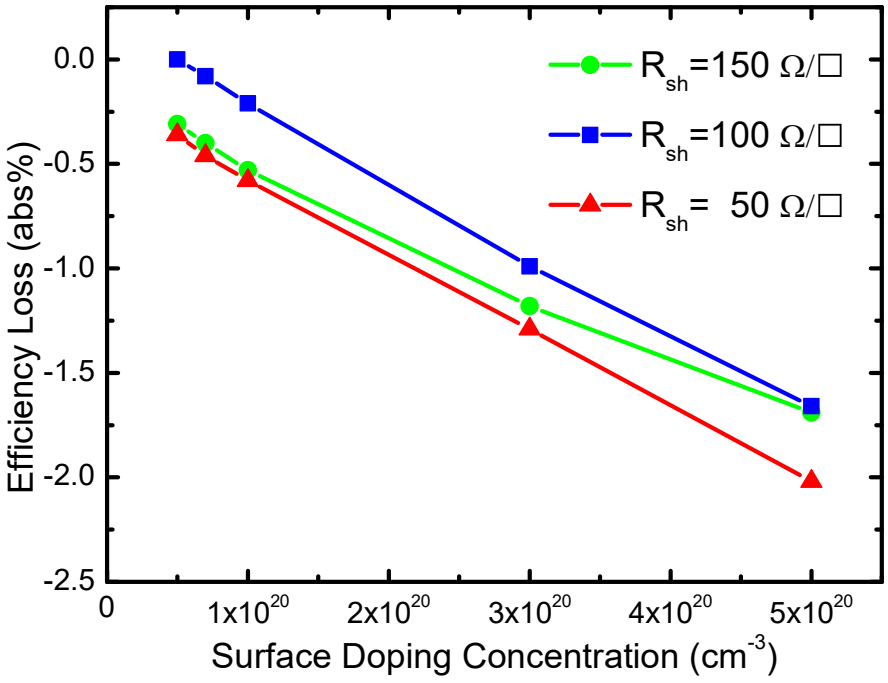

(b)

Fig. 6.6 (a) different doping profile with fixed sheet resistance 100 Ω/ (b) Efficiency loss as a function of surface doping concentration.

6.2.2 Substrate Doping

Due to the non-uniform distribution of dopant in a Si ingot, the wafers sliced from the same ingot have a range of resistivity. Thus, substrate doping concentration is a variable which affects bulk recombination. In this simulation, the substrate resistivity range considered is 1–5 Ω-cm corresponding to 2.75×10^{15}–1.5×10^{16} cm^3 in doping concentration. The corresponding minority carrier lifetime is 120–235 μs. The simulation examines the combined effect of substrate doping and diffusion temperature, where the temperature range is 770–900˚C. The result is shown in Fig. 6.7.

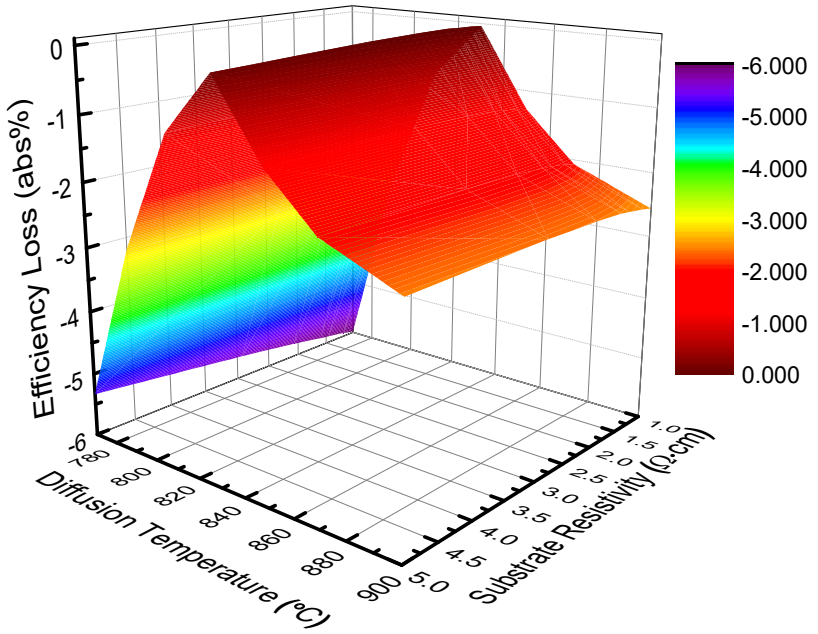

Fig. 6.7 Efficiency loss as a function of substrate doping and diffusion temperature.

Compared to diffusion temperature, substrate doping has less effect on cell efficiency. At 830˚C, the efficiency loss in the entire range of substrate doping (2.75×10^{15}–1.5×10^{16} cm^3) is less than 0.15% absolute. This means that diffusion temperature plays a dominant role over substrate doping in cell efficiency. Therefore, it is important to maintain a uniform temperature profile in a diffusion furnace for efficiency uniformization.

6.2.3 Finger Electrode Width

The width of the front electrode is prone to variation as screen printing is not as accurate as lithography. Ambient conditions and Ag paste are also possible reasons for the variation. A wider finger gives a smaller finger resistance but a larger shadow. Accurately evaluating the effect of electrode width on cell efficiency requires 3-D numerical simulations, which are time-consuming. In this study, a lumped finger resistance is added in the 2-D simulation. The formula for finger resistance is [77]:

$$R_{finger} = \frac{\rho L}{3tW} \tag{6.1}$$

where ρ is the resistivity of the finger, taken as 3×10^{-6} Ω-cm. L is the finger length, W is the finger width and t is the finger thickness. t is ~25μm. For a 156×156 mm^2 two-busbar cell, L=38 mm. The range for W is set to be 60–180μm. The cell structure simulated is in Fig. 7 except that the finger width W changes. The contact resistivity is fixed to 1×10^{-5} Ω-cm^2. The result is shown in Fig. 6.8.

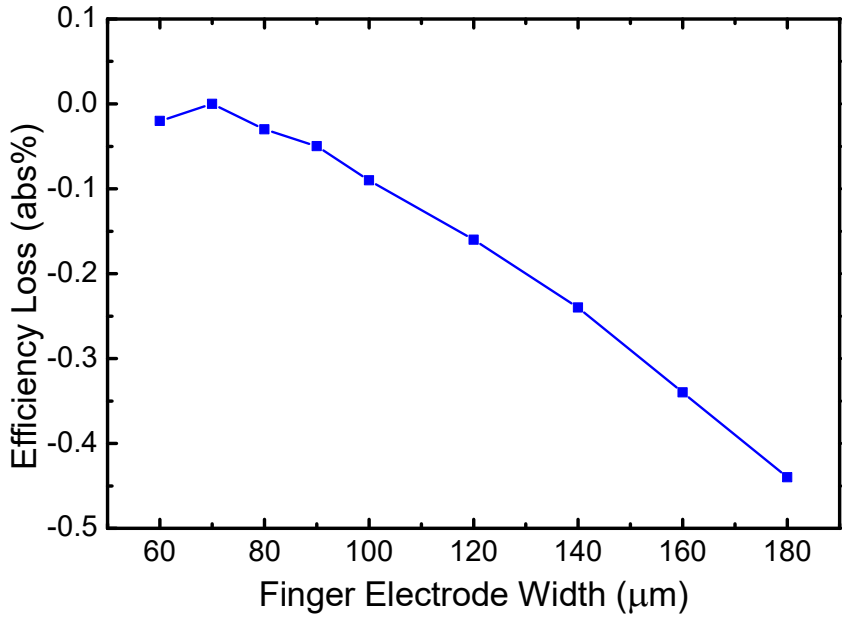

Fig. 6.8 Efficiency loss as a function of finger electrode width.

As the finger electrode width increases from 70μm to 180μm, the efficiency loss is ~0.45% absolute. Below 70μm, the efficiency goes down with finger width. For fingers below 70μm, we have to improve the Ag paste for a lower resistivity or increase the aspect ratio of the finger to maintain a high efficiency.

6.2.4 Discussions

The simulations presented above quantify the contribution from each of the process variables: diffusion temperature, substrate doping and finger electrode width, to cell

efficiency dispersion. Table 6.2 summarizes the results. Diffusion temperature is no doubt the dominant factor in cell efficiency dispersion. A 5× change in substrate doping has a negligible effect on cell efficiency. The variation in finger electrode width is typically in the ±20 μm range, which also has a small effect on cell efficiency.

Table 6.2 Efficiency loss due to various process variables

Variable	Range	Δη (abs%)
Diffusion temperature	770–830˚C	5.9
Substrate doping	1–5 Ω-cm	0.15
Finger electrode width	60–180 μm	0.43

Diffusion temperature is the key process variable to control. Table 6.3 summarizes factors which are related to diffusion and their individual effect on cell efficiency. Emitter resistance is the key factor on cell efficiency, while emitter recombination plays a secondary role.

Table 6.3 Efficiency loss due to factors related to diffusion

Factor	Range	Δη (abs%)
Contact resistivity	10^{-7}–10^{-3} Ω-cm^2	0.1
Emitter resistance	40–1750 Ω/□	8.5
Emitter recombination	5×10^{19}–5×10^{20} cm^{-3}	1.66

6.3 Efficiency Dispersion Control

Efficiency dispersion control requires the efficiency fluctuation in the production of solar cells is limited to a small range. Since doping temperature is the key sensitive process parameter to final efficiency, it should be also restricted to a certain range. To determine this temperature range, quantitative effects of the other parameters with reasonable discrepancies are to be evaluated first, which take up a certain amount of efficiency variation room, then the rest of room is left for temperature fluctuation. In this work, the efficiency control target is 1% absolute between the highest and lowest efficiencies which a fixed structure solar cell can reach. The standard solar cell is set to be the best performance (18.72%) one in last section, with the main dimension parameters equal to those in Table I and the phosphorus profile obtained at doping temperature 830 ℃. Each parameter is analyzed below respectively by replacing the standard value with a reasonable range of values.

6.3.1 Substrate doping concentration

Silicon wafers selling in the PV market are commonly marked with resistivity 1~3 Ω-cm or 3~6 Ω-cm [78]. Taking the former one as the primary wafers, the substrate doping concentration varies from 4.68×10^{15} to 1.51×10^{16} cm^{-3}. The efficiency as a function of substrate resistivity is shown in Fig. 6.9, in which the highest efficiency is 18.72% at 1.5 Ω-cm while the lowest one is 18.69% at 1Ω-cm. The efficiency difference is 0.03% absolute.

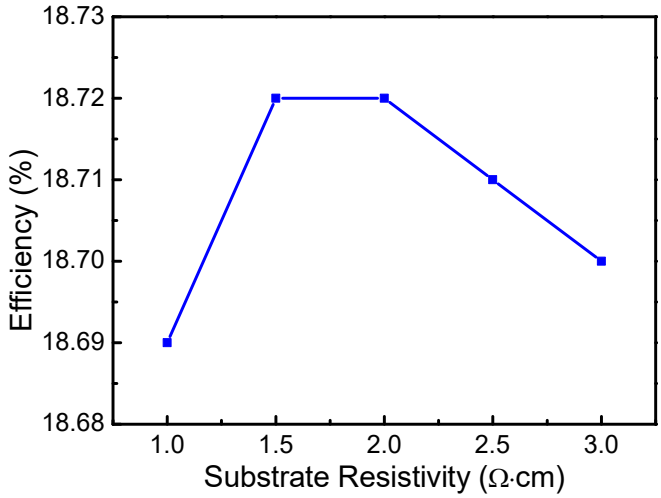

Fig. 6.9 Efficiency as a function of substrate resistivity

6.3.2 Front side finger width

The metal fingers on the front side of solar cell are fabricated by screen printing. The resolution of an advanced screen printer is ~8μm [79], so the variation of finger width could be ±15μm considering the deformation of silver lines during firing process. Hence, the finger width range is 55~85μm. The efficiency as a function of finger width is shown in Fig. 6.10, in which the highest efficiency is 18.73% at 85μm while the lowest one is 18.62% at 55μm. The efficiency difference is 0.11% absolute.

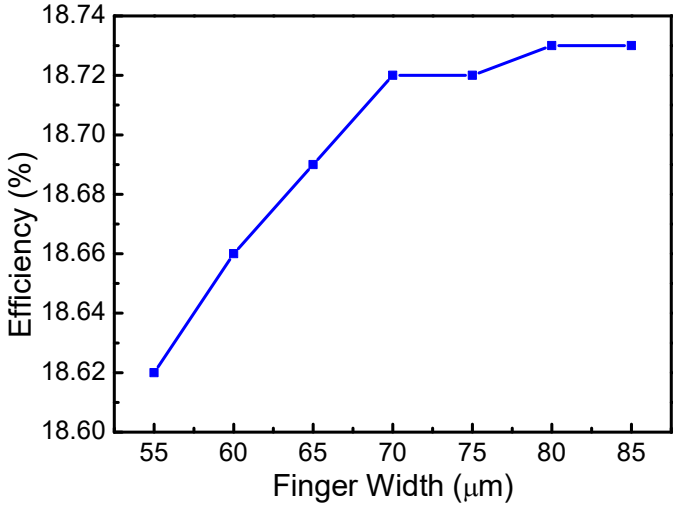

Fig. 6.10 Efficiency as a function of finger width

6.3.3 Front side finger thickness

There is no official technique data about the percentage of finger thickness changes during firing, so an estimated ±20% variation is applied in this part, which gives finger thickness of the range 20~30μm. The efficiency as a function of finger thickness is shown in Fig. 17, in which the highest efficiency is 18.82% at 30μm while the lowest one is 18.57% at 20μm. The efficiency difference is 0.25% absolute.

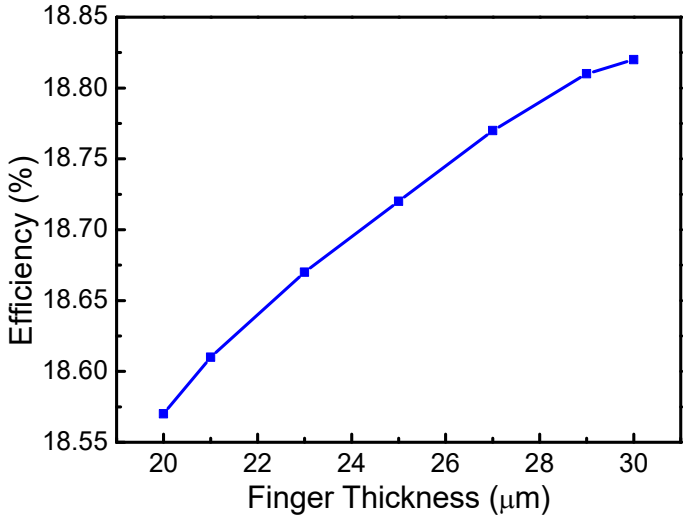

Fig. 6.11 Efficiency as a function of finger thickness.

6.3.4 ARC thickness

Anti-reflection coating (ARC) layer is ~75nm deposited by PECVD process. Since PECVD is a mature process, the error of thickness is well controlled down to 5nm. Thus the range of ARC thickness is 70~80nm. The efficiency as a function of ARC layer thickness is shown in Fig. 6.12, in which the highest efficiency is 18.73% at 73nm while the lowest one is 18.65% at 80nm. The efficiency difference is 0.08% absolute.

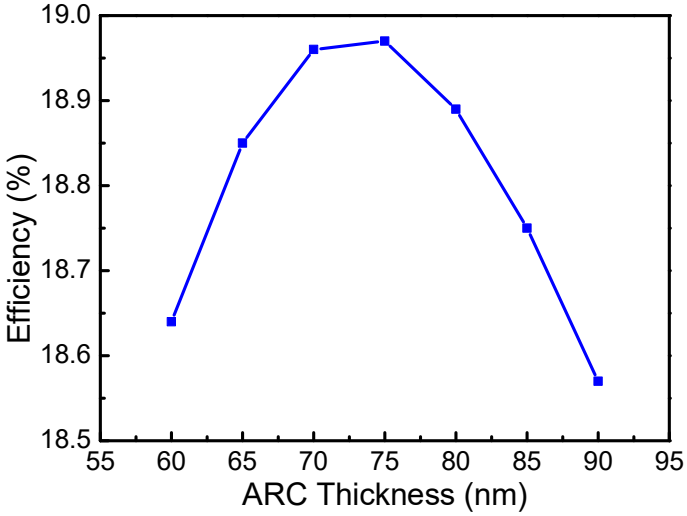

Fig. 6.12 Efficiency as a function of ARC thickness.

6.3.5 Diffusion temperature

Diffusion temperature is the most sensitive factor which has effects on several parameters and then changes the final efficiency. As all the variation of the other factors are studied, the most positive and negative cases combined with their effects on efficiency are obtained and listed in Table 6.4.

Table 6.4 Most positive and negative cases

Factor	Positive to η	Negative to η	Δη (abs%)
Substrate Resist.(Ω-cm)	1.5	1	0.03
Finger Width (um)	80	55	0.11
Finger Thickness (um)	30	20	0.25
ARC Thickness (nm)	73	80	0.08
Efficiency η(%)	18.82	18.35	0.47

As shown above, since the best case always stays with the diffusion temperature at 830℃ unable to improve, in the worst case there is still 0.53% absolute in efficiency allowed for diffusion temperature variation.

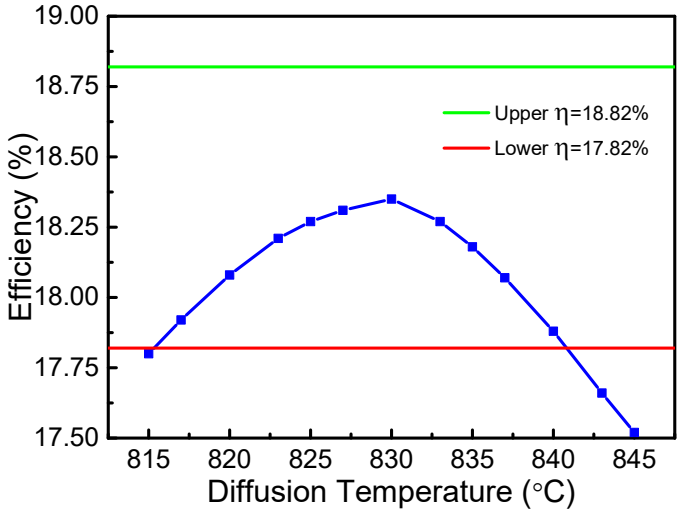

Fig. 6.13 Efficiency as a function of diffusion temperature with worst case.

From the result in Fig. 6.13, the allowed temperature range is around 815~840 ℃. Hence, the solar cell efficiency dispersion could be controlled within 1% absolute provided that the doping temperature fluctuates with this certain range.

Temperature variations in diffusion furnaces come from the fact that room-temperature $POCl_3/N_2$ are introduced into a hot zone of ~850˚C, causing a temperature gradient for the wafers. For efficiency uniformization, the room-temperature gases should be preheated before entering the furnace to reduce the temperature gradient. Alternatively, inline diffusion has a much smaller spread in emitter sheet resistance.

6.4 Summary

A comprehensive sensitivity analysis is presented to understand the efficiency dispersion in production of crystalline-Si solar cells. Using numerical simulations, the effects of diffusion temperature, substrate doping and finger electrode width on cell efficiency are quantified. It is found that diffusion temperature has a dominant effect on cell efficiency. Moreover, factors related to diffusion such as contact resistance, emitter

resistance and emitter recombination are evaluated for their individual effect on cell efficiency. Resistive losses in the emitter are primarily responsible for efficiency dispersion. Finally, considering all the device parameters related to process with reasonable variation, the cell efficiency fluctuation can be controlled within 1% absolute on condition that the doping temperature is stable within the range 815~840 ℃. Approaches for efficiency uniformization are proposed including preheating the gases and inline diffusion.

7. CONCLUSION AND OUTLOOK

7.1 Conclusion

This work focuses on the path to reduce the cost of industrial silicon solar cell manufacturing. Since the cutting-edge Ag screen printing method has bottlenecks for terawatt-level photovoltaic application because of the high price and limited reservation of Ag, alternative metallization technology with an earth-abundant low-cost highly-conductive metal is on demand in the future. Room temperature Al electroplating is proposed as a promising solution to this issue on front contact metallization. Starting from a half-processed p-type industrial Si solar cell substrate, an all-Al Si solar cell is fabricated with the electroplated Al front electrode in the ionic liquid. Additional annealing is performed to improve the contact resistance. Though this cell has a relatively low 14.6% efficiency, it proves the feasibility of Al electroplating for Si solar cell front electrode metallization. In order to avoid the shunting issues observed in the p-type cell, an n-type cell with rear junction structure is designed and carried out with the same method. The efficiency reaches 17.9% and is comparable to a same-structure screen-printed Ag electrode Si solar cell from industrial production lines. The modified cell shows an excellent spiking resistant characteristic compared to the traditional p-type solar cell.

Due to the limitation from the high-resistive solar grade Si substrate, conventional electroplating of Al for solar cell metallization requires a seed layer to deliver the current to all the fingers, thus it fails to take the advantage of the compatibility between Al and Si. In order to simplify the process and further reduce the cost, the light-induced plating is introduced and first achieved to deposit Al direct on Si surface without a Ni seed layer. The plated Al is continuous and dense with good adhesion to the Si surface. The low resistivity

down to 10^{-6} Ω-cm level fulfills the requirement for front electrode metallization. A new tool is designed and implemented to improve the reliability and repeatability of this process. The modified design can be extended to full-size solar cell manufacturing and mass production. The methods to determine the light source and monitor ion concentration are also proposed. This work further confirms Al as the promising candidate to replace Ag in PV industry.

A secondary topic on Si solar cell efficiency uniformization analysis is presented. With a numerical simulation in Sentaurus, phosphorus diffusion process is extracted to be the main factor leading to efficiency dispersion. Relative factors to diffusion are also evaluated and compared with each other. Taking the whole fabrication process into account, possible variations in each step are introduced to the efficiency simulation. The goal to control the efficiency fluctuation within 1% is achievable if the doping temperature is stable within the range 815~840ºC. Approaches to improve efficiency uniformization are proposed.

7.2 Outlook

As the light-induced plating of Al in the ionic liquid is achieved, it is natural to extend this method to solar cell fabrication and then industrial production. In the future, there are still issues requiring investigation.

First, it is necessary to find a way to improve the uniformity of Al layer on the solar cell surface. Though light-induced plating can achieve uniform deposition, the textured rough Si surface is always a challenge. Electroplating is a subtle and complicated process requiring a flat and clean substrate surface. However, the solar cell samples employed here go through different processes including texturing and laser ablation, which changes the

surface morphology and could introduce damage or contamination. Hence, it is difficult to ensure the uniformity of the deposited metal layer. Some literature reported that organic additives help uniform plating on metals [80-83], but it is unclear for Si substrate. Changing the current source from DC to AC may also improve the uniformity [84, 85].

Second, the contact resistivity between light-induced plated Al and Si requires investigation. In conventional electroplating, Ni seed layer with follow-up annealing forms Ni silicide to reduce the contact resistance. However, it is not suitable to perform annealing for Al-Si system as Al will spike into the n^+-Si emitter and destroy the p-n junction. Meanwhile, considering the NaOH cleaning is employed to remove damage, a layer of the n^+ surface is etched off. The metal-semiconductor requires a highly doped surface to form an Ohmic contact. In this case, the NaOH etching should be carefully controlled to maintain a high doping concentration surface.

Third, designing a tool to fit 6-inch solar cell wafers is challenging. Though the ionic liquid is stable at room temperature, it is sensitive to water and moisture, so this process cannot be carried out in a room environment. One possible solution is heating the ionic liquid above 100ºC to drive out and prevent moisture. This method worked well in a small beaker as the container. However, when it changed to a wide-opening container, I can smell a strong odor if the temperature was above 70ºC, thus further respiratory protection is required. This will be an extra-large amount of cost in mass production. There are some new air and water stable ionic liquids developed to lower the experimental requirement [86-88], so it is possible to introduce new electrolyte for this process.

REFERENCES

[1] I. P. o. C. Change, *Climate Change 2014–Impacts, Adaptation and Vulnerability: Regional Aspects*: Cambridge University Press, 2014.

[2] J. Rogelj, M. Den Elzen, N. Höhne, T. Fransen, H. Fekete, H. Winkler*, et al.*, "Paris Agreement climate proposals need a boost to keep warming well below 2 C," *Nature,* vol. 534, pp. 631-639, 2016.

[3] U. E. I. Administration, "International Energy Outlook," *Outlook,* 2017.

[4] Itrpv, "International Technology Roadmap for Photovoltaic," 2017.

[5] L. Frantzis, E. Jones, C. Lee, M. Wood, and P. Wormser, "Opportunities for cost reductions in photovoltaic modules," in *16th European Photovoltaic Solar Energy Conference*, 2000, pp. 2100-2103.

[6] http://pvinsights.com/index.php.

[7] http://www.macrotrends.net/1470/historical-silver-prices-100-year-chart.

[8] U. S. G. Survey, "Silver," *Mineral Commodity Summaries,* pp. 2016-2017, 2017.

[9] J. A. Ober, "Mineral commodity summaries 2017," US Geological Survey2017.

[10] http://pveducation.org/pvcdrom.

[11] M. Tao, *Terawatt solar photovoltaics: roadblocks and opportunities*: Springer, 2014.

[12] R. M. Swanson, "Approaching the 29% limit efficiency of silicon solar cells," in *Photovoltaic Specialists Conference, 2005. Conference Record of the Thirty-first IEEE*, 2005, pp. 889-894.

[13] M. A. Green, "Silicon solar cells: state of the art," *Philosophical Transactions of*

the Royal Society a-Mathematical Physical and Engineering Sciences, vol. 371, Aug 2013.

[14] http://www.yinglisolar.com/us/products/monocrystalline/.

[15] W.-C. Sun, *Development of Silver-Free Silicon Photovoltaic Solar Cells with All-Aluminum Electrodes*: Arizona State University, 2016.

[16] D. D. Smith, P. Cousins, S. Westerberg, R. De Jesus-Tabajonda, G. Aniero, and Y.-C. Shen, "Toward the practical limits of silicon solar cells," *IEEE Journal of Photovoltaics,* vol. 4, pp. 1465-1469, 2014.

[17] A. Mette, *New concepts for front side metallization of industrial silicon solar cells*, 2007.

[18] L. B. William, G. C. Michael, B. H. Cynthia, and A. L. Israel, "United States Patent: 4137123 - Texture etching of silicon: method," 1979.

[19] https://www.pv-tech.org/products/schmid-offers-low-cost-pre-treatment-for-texturing-diamond-wire-cut-multi-c.

[20] J. Oh, H.-C. Yuan, and H. M. Branz, "An 18.2%-efficient black-silicon solar cell achieved through control of carrier recombination in nanostructures," *Nature nanotechnology,* vol. 7, pp. 743-748, 2012.

[21] H.-C. Yuan, V. E. Yost, M. R. Page, P. Stradins, D. L. Meier, and H. M. Branz, "Efficient black silicon solar cell with a density-graded nanoporous surface: optical properties, performance limitations, and design rules," *Applied Physics Letters,* vol. 95, p. 123501, 2009.

[22] H. Savin, P. Repo, G. Von Gastrow, P. Ortega, E. Calle, M. Garín, *et al.*, "Black silicon solar cells with interdigitated back-contacts achieve 22.1% efficiency," *Nature nanotechnology,* vol. 10, pp. 624-628, 2015.

[23] Y. Liu, T. Lai, H. Li, Y. Wang, Z. Mei, H. Liang, *et al.*, "Nanostructure formation

and passivation of large-area black silicon for solar cell applications," *Small,* vol. 8, pp. 1392-1397, 2012.

[24] https://archive.cnx.org/contents/9583ee74-d153-4059-9239-5976da5a9589@2/chapter-6-ic-fabrication-technology-from-60s-to-date-part-1.

[25] https://schmid-group.com/en/markets/photovoltaics/cell/edge-isolation-psg-etching/.

[26] https://www.rena.com/solutions/product/cell-front-end-batch/batchox/.

[27] https://www.rena.com/solutions/product/cell-front-end-inline/inoxsideR/.

[28] M. Ju, Y.-J. Lee, J. Lee, B. Kim, K. Ryu, K. Choi*, et al.*, "Double screen printed metallization of crystalline silicon solar cells as low as 30μm metal line width for mass production," *Solar Energy Materials and solar cells,* vol. 100, pp. 204-208, 2012.

[29] M. Galiazzo, V. Furin, D. Tonini, G. Cellere, and A. Baccini, "Double printing of front contact Ag in c-Si solar cells," in *Proceedings of the 25th European Photovoltaic Solar Energy Conference, Valencia, Spain*, 2010, pp. 6-10.

[30] A. W. Blakers, A. Wang, A. M. Milne, J. Zhao, and M. A. Green, "22.8% efficient silicon solar cell," *Applied Physics Letters,* vol. 55, pp. 1363-1365, 1989.

[31] E. Schneiderlöchner, R. Preu, R. Lüdemann, and S. Glunz, "Laser-fired rear contacts for crystalline silicon solar cells," *Progress in Photovoltaics: Research and Applications,* vol. 10, pp. 29-34, 2002.

[32] J. Schmidt, A. Merkle, R. Brendel, B. Hoex, M. Van De Sanden, and W. Kessels, "Surface passivation of high-efficiency silicon solar cells by atomic-layer-deposited Al2O3," *Progress in photovoltaics: research and applications,* vol. 16, pp. 461-466, 2008.

[33] P. Saint-Cast, J. Benick, D. Kania, L. Weiss, M. Hofmann, J. Rentsch*, et al.*, "High-

efficiency c-Si solar cells passivated with ALD and PECVD aluminum oxide," *IEEE Electron Device Letters,* vol. 31, pp. 695-697, 2010.

[34] S. M. Sze and K. K. Ng, *Physics of semiconductor devices*: John wiley & sons, 2006.

[35] S. M. Sze, *Semiconductor devices: physics and technology*: John Wiley & Sons, 2008.

[36] J. Murray and A. McAlister, "The Al-Si (aluminum-silicon) system," *Journal of Phase Equilibria,* vol. 5, pp. 74-84, 1984.

[37] H. Mii, M. Senoo, and I. Fujishiro, "Solid solubility of Si in Al under high pressure," *Japanese Journal of Applied Physics,* vol. 15, p. 777, 1976.

[38] J. McCaldin and H. Sankur, "Diffusivity and solubility of Si in the Al metallization of integrated circuits," *Applied physics letters,* vol. 19, pp. 524-527, 1971.

[39] D.-H. Neuhaus, #252, and A. nzer, "Industrial Silicon Wafer Solar Cells," *Advances in OptoElectronics,* vol. 2007, 2007.

[40] M. Kessler, D. Münster, T. Neubert, C. Mader, J. Schmidt, and R. Brendel, "High-efficiency back-junction silicon solar cell with an in-line evaporated aluminum front grid," in *Photovoltaic Specialists Conference (PVSC), 2011 37th IEEE*, 2011, pp. 001085-001090.

[41] P. A. Basore, E. Van Kerschaver, K. Cabanas-Holmen, J. Hummel, Y. Lin, C. P. Murcia*, et al.*, "All-aluminum screen-printed IBC cells: Design concept," in *Photovoltaic Specialists Conference (PVSC), 2013 IEEE 39th*, 2013, pp. 0900-0903.

[42] R. T. Carlin, W. Crawford, and M. Bersch, "Nucleation and Morphology Studies of Aluminum Deposited from an Ambient-Temperature Chloroaluminate Molten Salt," *Journal of The Electrochemical Society,* vol. 139, pp. 2720-2727, 1992.

[43] Q. Liao, W. R. Pitner, G. Stewart, C. L. Hussey, and G. R. Stafford,

"Electrodeposition of aluminum from the aluminum chloride-1-methyl-3-ethylimidazolium chloride room temperature molten salt+ benzene," *Journal of the Electrochemical Society,* vol. 144, pp. 936-943, 1997.

[44] J. J. Lee, I. T. Bae, D. A. Scherson, B. Miller, and K. A. Wheeler, "Underpotential deposition of aluminum and alloy formation on polycrystalline gold electrodes from AlCl3/EMIC room-temperature molten salts," *Journal of The Electrochemical Society,* vol. 147, pp. 562-566, 2000.

[45] A. P. Abbott, C. A. Eardley, N. R. Farley, G. A. Griffith, and A. Pratt, "Electrodeposition of aluminium and aluminium/platinum alloys from AlCl 3/benzyltrimethylammonium chloride room temperature ionic liquids," *Journal of Applied Electrochemistry,* vol. 31, pp. 1345-1350, 2001.

[46] L. Wang, H. Zhang, W.-C. Sun, and M. Tao, "Efficiency dispersion in production of crystalline-Si solar cells by numerical simulation," in *Photovoltaic Specialist Conference (PVSC), 2015 IEEE 42nd*, 2015, pp. 1-5.

[47] W.-C. Sun, X. Han, and M. Tao, "Electroplating of aluminium on silicon in an ionic liquid," *ECS Electrochemistry Letters,* vol. 4, pp. D5-D7, 2015.

[48] W.-C. Sun, H. Zhang, L. Wang, C. J. Tracy, and M. Tao, "Electroplated Al as the front electrode in crystalline-Si solar cells," in *Photovoltaic Specialist Conference (PVSC), 2015 IEEE 42nd*, 2015, pp. 1-5.

[49] W.-C. Sun, X. Han, H. Zhang, C. J. Tracy, and M. Tao, "Non-vacuum electroplated Al for n-side electrode in Si solar cells," in *Photovoltaic Specialist Conference (PVSC), 2014 IEEE 40th*, 2014, pp. 2533-2537.

[50] G. J. Janz, *Molten salts handbook*: Elsevier, 2013.

[51] G. Capuano, "Plating aluminum onto steel or copper from alkyl benzene electrolytes," *Plating,* vol. 60, pp. 251-255, 1973.

[52] L. Legrand, A. Tranchant, and R. Messina, "Behaviour of aluminium as anode in

dimethylsulfone-based electrolytes," *Electrochimica acta,* vol. 39, pp. 1427-1431, 1994.

[53] T. Welton, "Room-Temperature Ionic Liquids. Solvents for Synthesis and Catalysis," *Chemical Reviews,* vol. 99, pp. 2071-2084, 1999/08/11 1999.

[54] M. Zhang, V. Kamavarum, and R. G. Reddy, "New electrolytes for aluminum production: Ionic liquids," *JOM,* vol. 55, pp. 54-57, 2003.

[55] T. Jiang, M. J. Chollier Brym, G. Dubé, A. Lasia, and G. M. Brisard, "Electrodeposition of aluminium from ionic liquids: Part I—electrodeposition and surface morphology of aluminium from aluminium chloride (AlCl3)–1-ethyl-3-methylimidazolium chloride ([EMIm]Cl) ionic liquids," *Surface and Coatings Technology,* vol. 201, pp. 1-9, 2006.

[56] T. Jiang, M. J. Chollier Brym, G. Dubé, A. Lasia, and G. M. Brisard, "Electrodeposition of aluminium from ionic liquids: Part II - studies on the electrodeposition of aluminum from aluminum chloride (AICl3) - trimethylphenylammonium chloride (TMPAC) ionic liquids," *Surface and Coatings Technology,* vol. 201, pp. 10-18, 2006.

[57] C. Lavoie, F. d'Heurle, C. Detavernier, and C. Cabral, "Towards implementation of a nickel silicide process for CMOS technologies," *Microelectronic Engineering,* vol. 70, pp. 144-157, 2003.

[58] J. Karas, S. Kim, L. Michaelson, K. Munoz, T. Tyson, and S. Bowden, "Electrical characterization of thermally-formed nickel silicide for nickel-copper plated solar cell contacts," in *Photovoltaic Specialist Conference (PVSC), 2015 IEEE 42nd*, 2015, pp. 1-5.

[59] L. F. Durkee, "United States Patent: 4144139 - Method of plating by means of light," ed, 1979.

[60] L. A. Grenon, " United States Patent: 4251327 - Electroplating method," ed, 1981.

[61] A. Lennon, Y. Yao, and S. Wenham, "Evolution of metal plating for silicon solar cell metallisation," *Progress in Photovoltaics: Research and Applications,* vol. 21, pp. 1454-1468, 2013.

[62] E.-J. Lee, D. Kim, and S. Lee, "Ni/Cu metallization for low-cost high-efficiency PERC cells," *Solar energy materials and solar cells,* vol. 74, pp. 65-70, 2002.

[63] A. Mette, C. Schetter, D. Wissen, S. Lust, S. Glunz, and G. Willeke, "Increasing the efficiency of screen-printed silicon solar cells by light-induced silver plating," in *Photovoltaic Energy Conversion, Conference Record of the 2006 IEEE 4th World Conference on*, 2006, pp. 1056-1059.

[64] J. Bartsch, V. Radtke, C. Schetter, and S. Glunz, "Electrochemical methods to analyse the light-induced plating process," *Journal of Applied Electrochemistry,* vol. 40, pp. 757-765, 2010.

[65] S. W. Glunz, J. Knobloch, D. Biro, and W. Wettling, "Optimized high-efficiency silicon solar cells with JSC=42 mA/cm2 and η= 23.3% " presented at the European Photovoltaic Solar Energy Conference, Barcelona, 1997.

[66] N. Bay, V. Radtke, M. Aleman, J. Bartsch, and S. W. Glunz, "Electrolytic Nickel Deposition for the Front Side Metallization of Silicon Solar," *24th European Photovoltaic Solar Energy Conference,* pp. 1434-1436, 2009.

[67] J. Bartsch, A. Mondon, M. Kamp, A. Kraft, M. Wendling, M. Mehling*, et al.*, "Progress with multi-step metallization processes featuring copper as conducting layer at Fraunhofer ISE," in *Proceedings of 27th European Photovoltaic Solar Energy Conference and Exhibition*, 2012, p. 604.

[68] B. Hallam, S. Wenham, A. Sugianto, L. Mai, C. Chong, M. Edwards*, et al.*, "Record large-area p-type CZ production cell efficiency of 19.3% based on LDSE technology," *IEEE Journal of Photovoltaics,* vol. 1, pp. 43-48, 2011.

[69] L. Tous, J. F. Lerat, T. Emeraud, R. Negru, K. Huet, A. Uruena*, et al.*, "Nickel silicide contacts formed by excimer laser annealing for high efficiency solar cells,"

Progress in Photovoltaics: Research and Applications, vol. 21, pp. 267-275, 2013.

[70] D. Kyeong, S. Cho, J. Lim, K. Lee, M. Hwang, W. Lee*, et al.*, "Approaching 20%-efficient selective-emitter solar cells with copper front contacts on industrial 156 mm Cz Si wafers," in *Proceedings of the 27th European Photovoltaic Solar Energy Conference and Exhibition*, 2012.

[71] W.-H. Huang, W. J. Shin, L. Wang, W.-C. Sun, and M. Tao, "Strategy and technology to recycle wafer-silicon solar modules," *Solar Energy,* vol. 144, pp. 22-31, 2017.

[72] K. C. Leadbetter, "Advances in the electrodeposition of aluminum from ionic liquid based electrolytes," Master, University of North Dakota, 2014.

[73] A. Bentzen, J.S. Christensen, and a. A. H. B.G. Svensson, "Understanding phosphorus emitter diffusion in silicon solar cell processing," in *21st European Photovoltaic Solar Energy Conference*, 2006, pp. 1388-1391.

[74] P. P. Altermatt, "Models for numerical device simulations of crystalline silicon solar cells—a review," *Journal of computational electronics,* vol. 10, p. 314, 2011.

[75] G. Micard, A. Dastgheib-Shirazi, B. Raabe, and G. Hahn, "Diffusivity Analysis of POCl3 Emitter SIMS Profiles for Semi Empirical Parametrization in Sentaurus Process," in *26th European Photovoltaic Solar Energy Conference and Exhibition*, Hamburg, 2011, pp. 1446 - 1450.

[76] D. K. Schroder and D. L. Meier, "Solar cell contact resistance—a review," *IEEE Transactions on electron devices,* vol. 31, pp. 637-647, 1984.

[77] A. Goetzberger, J. Knobloch, and B. Voss, *Crystalline silicon solar cells*: Wiley Online Library, 1998.

[78] http://www.ldksolar.com/pro_wafer_mon.php.

[79] http://www.appliedmaterials.com/files/Applied-Baccini-Cell-Systems-

Brochure_en.pdf.

[80] F. Endres, M. Bukowski, R. Hempelmann, and H. Natter, "Electrodeposition of nanocrystalline metals and alloys from ionic liquids," *Angewandte Chemie International Edition,* vol. 42, pp. 3428-30, Jul 28 2003.

[81] L. Barchi, U. Bardi, S. Caporali, M. Fantini, A. Scrivani, and A. Scrivani, "Electroplated bright aluminium coatings for anticorrosion and decorative purposes," *Progress in Organic Coatings,* vol. 68, pp. 120-125, 2010.

[82] L. Liu, X. Lu, Y. Cai, Y. Zheng, and S. Zhang, "Influence of Additives on the Speciation, Morphology, and Nanocrystallinity of Aluminium Electrodeposition," *Australian Journal of Chemistry,* vol. 65, p. 1523, 2012.

[83] Q. Zhang, Q. Wang, S. Zhang, and X. Lu, "Effect of nicotinamide on electrodeposition of Al from aluminium chloride (AlCl3)-1-butyl-3-methylimidazolium chloride ([Bmim]Cl) ionic liquids," *Journal of Solid State Electrochemistry,* vol. 18, pp. 257-267, 2013.

[84] B. Li, C. Fan, Y. Chen, J. Lou, and L. Yan, "Pulse current electrodeposition of Al from an AlCl3-EMIC ionic liquid," *Electrochimica Acta,* vol. 56, pp. 5478-5482, 2011.

[85] J. Tang and K. Azumi, "Optimization of pulsed electrodeposition of aluminum from AlCl3-1-ethyl-3-methylimidazolium chloride ionic liquid," *Electrochimica Acta,* vol. 56, pp. 1130-1137, 2011.

[86] S. Zein El Abedin, E. Moustafa, R. Hempelmann, H. Natter, and F. Endres, "Additive free electrodeposition of nanocrystalline aluminium in a water and air stable ionic liquid," *Electrochemistry Communications,* vol. 7, pp. 1111-1116, 2005.

[87] M. Armand, F. Endres, D. R. MacFarlane, H. Ohno, and B. Scrosati, "Ionic-liquid materials for the electrochemical challenges of the future," *Nature materials,* vol. 8, pp. 621-629, 2009.

[88] S. Zein El Abedin, E. Moustafa, R. Hempelmann, H. Natter, and F. Endres, "Electrodeposition of Nano-and Microcrystalline Aluminium in Three Different Air and Water Stable Ionic Liquids," *ChemPhysChem,* vol. 7, pp. 1535-1543, 2006.